Broadband Trailing-Edge Noise Predictions. Overview of BANC-III Results

(Article begins on next page)

02 September 2025

Broadband Trailing-Edge Noise Predictions— Overview of BANC-III Results

M. Herr[*], R. Ewert[†] and C. Rautmann[*]

German Aerospace Center (DLR), D-38108 Braunschweig, Germany

M. Kamruzzaman[‡]

Vestas Technology UK Ltd., Newport, PO30 5TR, United Kingdom

D. Bekiropoulos[§]

University of Stuttgart, D-70569 Stuttgart, Germany

A. Iob[¶]

wavePRO S.R.L., I-10129 Torino, Italy

R. Arina[‖]

Politecnico di Torino, I-10129 Torino, Italy

P. Batten[**] and S. Chakravarthy[††]

Metacomp Technologies, Inc., Agoura Hills, CA 91301, USA

F. Bertagnolio [‡‡]

DTU Wind Energy, Technical University of Denmark, DK-4000 Roskilde, Denmark

The Third Workshop on Benchmark Problems for Airframe Noise Computations, BANC-III, was held on 14–15 June 2014 in Atlanta, Georgia, USA. The objective of this workshop was to assess the present computational capability in the area of physics-based prediction of different types of airframe noise problems and to advance the state-of-the-art via a combined effort. This documentation summarizes the results from workshop category 1 which focuses on the prediction of broadband turbulent boundary-layer trailing-edge noise and related source quantities. Since the forerunner BANC-II workshop identified some room for improvements in the achieved prediction quality BANC-III relies on the same test cases, namely 2D NACA0012 and DU96-W-180 airfoil sections in a uniform flow.

Compared to BANC-II particularly the scatter among predictions for the DU96-W-180 test case could be significantly reduced. However, proposed adaptations of previously applied computational methods did not systematically improve the prediction quality for all requested parameters. The category 1 workshop problem remains a challenging simulation task due to its high requirements on resolving and modeling of turbulent boundary-layer source quantities.

[*]Research Scientists, DLR Institute of Aerodynamics and Flow Technology, Technical Acoustics, Lilienthalplatz 7, michaela.herr@dlr.de, christof.rautmann@dlr.de, AIAA Members.

[†]Senior Scientist, same affiliation, roland.ewert@dlr.de, AIAA Senior Member.

[‡]Specialist, Aeroacoustics, Vestas Technology UK Ltd., Noise, EMC & Vibrations, Technology & Service Solutions, West Medina Mills, Stag Lane, Newport, Isle of Wight, PO30 5TR, UK, MOKAM@vestas.com; formerly: Institute of Aerodynamics & Gas Dynamics (IAG), University of Stuttgart, Pfaffenwaldring 21, D-70569 Stuttgart, Germany.

[§]Research Scientist, Institute of Aerodynamics & Gas Dynamics (IAG), University of Stuttgart, Pfaffenwaldring 21, bekiropoulos@iag.uni-stuttgart.de.

[¶]Research Scientist, wavePRO S.R.L, andrea.iob@wavepro.eu.

[‖]Associate Professor, Dipartimento di Ingegneria Meccanica e Aerospaziale (DIMEAS), Politecnico di Torino, Corso Duca degli Abruzzi 24, renzo.arina@polito.it, AIAA Senior Member.

[**]Senior Scientist, Metacomp Technologies, Inc., 28632 Roadside Dr., batten@metacomptech.com, AIAA Senior Member.

[††]President, same affiliation, src@metacomptech.com.

[‡‡]Senior Scientist, DTU National Laboratory for Sustainable Energy, Wind Energy Department, Frederiksborgvej 399, frba@dtu.dk.

American Institute of Aeronautics and Astronautics

Nomenclature

Parameter definition and units

b	m	wetted airfoil span
c_f	-	wall friction coefficient, $c_f = \tau_w/(0.5\,\rho_\infty\,U_\infty^2)$
c_p	-	static pressure coefficient, $c_p = (p - p_\infty)/(0.5\,\rho_\infty\,U_\infty^2)$
c_∞	m/s	free stream speed of sound
f	Hz	(narrowband) frequency
f_c	Hz	1/3-octave band center frequency
G_{pp}	dB/Hz	single-sided PSD of unsteady surface pressures at TE (levels re 20 μPa)
k_i	1/m	hydrodynamic wave number in airfoil-fixed coordinates x_i (i = 1, 3)
k_T	m²/s²	specific kinetic energy of turbulence
$L_{p(1/3)}$	dB	1/3-octave band trailing-edge noise level (re 20 μPa)
l_c	m	chord length
M_∞	-	free stream Mach number
p	Pa	mean (surface) pressure
p_{rms}	Pa	root-mean-square sound pressure
p_∞	Pa	mean ambient pressure
r	m	distance between source position and observer (retarded coordinate system)
Re	-	chord-based Reynolds number
T_∞	K	ambient temperature
U_i	m/s	mean velocity components in airfoil-fixed coordinates x_i
u_i	m/s	fluctuating velocity components in airfoil-fixed coordinates x_i
$\mathbf{u}^t$	m/s	fluctuating solenoidal velocity component generated by FRPM
$\mathbf{u}^a$	m/s	fluctuating irrotational velocity component
$\mathbf{u}'$	m/s	fluctuating velocity component from CAA simulation $\mathbf{u}' = \mathbf{u}^t + \mathbf{u}^a$
$\mathbf{u}_0$	m/s	mean velocity component from CAA simulation $\mathbf{u}' = \mathbf{u}^t + \mathbf{u}^a$
U_c	m/s	turbulent eddy convection velocity
U_∞	m/s	mean free stream velocity
x_i	m	airfoil-fixed coordinates with origin at the leading edge at midspan (i = 1...3; 1: chordwise, 2: chord-normal, 3: spanwise), cf. figure 1
y^+	-	dimensionless wall-normal coordinate in inner TBL scaling
α	°	aerodynamical angle of attack
δ	m	TBL thickness at the TE
δ_1	m	TBL displacement thickness at the TE
δ_2	m	TBL momentum thickness at the TE
$\delta_{pq,kl}$	-	Kronecker delta
ϵ	m²/s³	isotropic turbulence mean dissipation rate
ϵ_{ijk}	-	Levi-Civita symbol
θ	°	TE observation angle in retarded coordinates, cf. figure 1
Λ	m	isotropic turbulence longitudinal integral length scale
Λ_2	m	abbreviate form for $\Lambda_{22}(x_2)$, i.e. correlation length scales derived from two-point correlation profiles of u_2 for probe separation coordinate in x_2-direction
ρ_∞	kg/m³	mean ambient density
τ_w	Pa	wall shear stress
ϕ	°	TE observation sideline angle in retarded coordinates, here: $\phi = 90°$
ϕ_m	s	'moving axis' spectrum
ω	rad/s	angular frequency, $\omega = 2\pi f$
ω_T	1/s	specific dissipation rate

Abbreviations, names

BANC	Benchmark Problems for Airframe Noise Computations
DLR	Deutsches Zentrum für Luft- und Raumfahrt (German Aerospace Center)
DTU	Danmarks Tekniske Universitet (Technical University of Denmark)
EllipSys2D	*in-house CFD software at DTU*
IAG	Institute of Aerodynamics & Gas Dynamics, University of Stuttgart
CAA	computational aeroacoustics
CFD	computational fluid dynamics
CFD^{++}	*CFD software package, Metacomp Technologies, Inc.*
FLOWer	*structured RANS solver, DLR*
FRPM	Fast Random Particle-Mesh Method *(synthetic turbulence method, DLR)*
FWH	Ffowcs-Williams-Hawkings *integration method for farfield noise prediction*
IDDES	Improved Delayed Detached Eddy Simulation
LES	Large-Eddy Simulation
LEST	Large-Eddy STtimulation *(synthetic turbulence method, Metacomp Technologies, Inc.)*
LWT	Laminar Wind-Tunnel, IAG
PIANO	Perturbation Investigation of Aerodynamic NOise *CAA solver, DLR)*
PoliTo	Politecnico di Torino *in cooperation with wavePRO S.R.L. and Metacomp Technologies, Inc.*
PS	pressure side
PSD	power spectral density
QCR	quadratic constitutive relations
RANS	Reynolds-averaged Navier-Stokes
Rnoise	RANS-based *TE* noise *prediction model, IAG Stuttgart*
SA	Spalart-Allmaras *turbulence model*
SS	suction side
SST	*Menter's* Shear Stress Transport *turbulence model*
TAU	*unstructured RANS solver, DLR*
(T)BL	(turbulent) boundary-layer
TE	trailing edge
TEN	turbulent boundary-layer trailing-edge noise
TNO	The Netherlands Organization of Applied Scientific Research

I.   Introduction

Since 2010, the American Institute of Aeronautics and Astronautics has organized an ongoing series of workshops dedicated to Benchmark Problems for Airframe Noise Computations (BANC). The BANC workshops are aimed at enabling a systematic progress in the understanding and high-fidelity predictions of airframe noise via collaborative investigations that integrate state of the art computational fluid dynamics (CFD), computational aeroacoustics (CAA), and comprehensive, holistic measurements in multiple facilities targeting a selected set of canonical yet realistic configurations.[11] For supplementary information the interested reader might refer to the BANC collaborative website.[1]

The current paper summarizes the previous year (2014) results from category 1 (BANC-III-1) devoted to turbulent boundary-layer trailing-edge (TBL-TE) noise or TEN in abbreviate form. To provide a continuous documentation of the incremental progress in this category the forerunner BANC-II-1 (2012) results have been previously published in 2013.[22]

As already experienced during BANC-I/II-1 mainly users of relatively fast hybrid prediction approaches submitted data for code-to-code comparisons and still, these contributions are less than representative of the broad TEN simulation community.

II.   Problem statement

Since the number of BANC-II category-1 participants was comparatively low (and some of the contributions were incomplete and/or showed room for further improvement) it was commonly agreed to repeat the workshop based on the BANC-II-1 NACA0012 and DU96-W-180 test cases #1–5 prior to go ahead with more sophisticated TEN simulation problems. Therefore, the remainder of this section is identical to what has been already written in the BANC-II-1 documentation.[22] Hurried readers who are familiar with the test cases might continue with section III.

The computation of flow and noise characteristics at sections of 2D airfoils in a nominally uniform stream, characterized by the mean velocity U_∞ and angle of attack α, according to figure 1 is solicited. Selected test cases are summarized in table 1. The definition of these cases has been based on cross comparisons
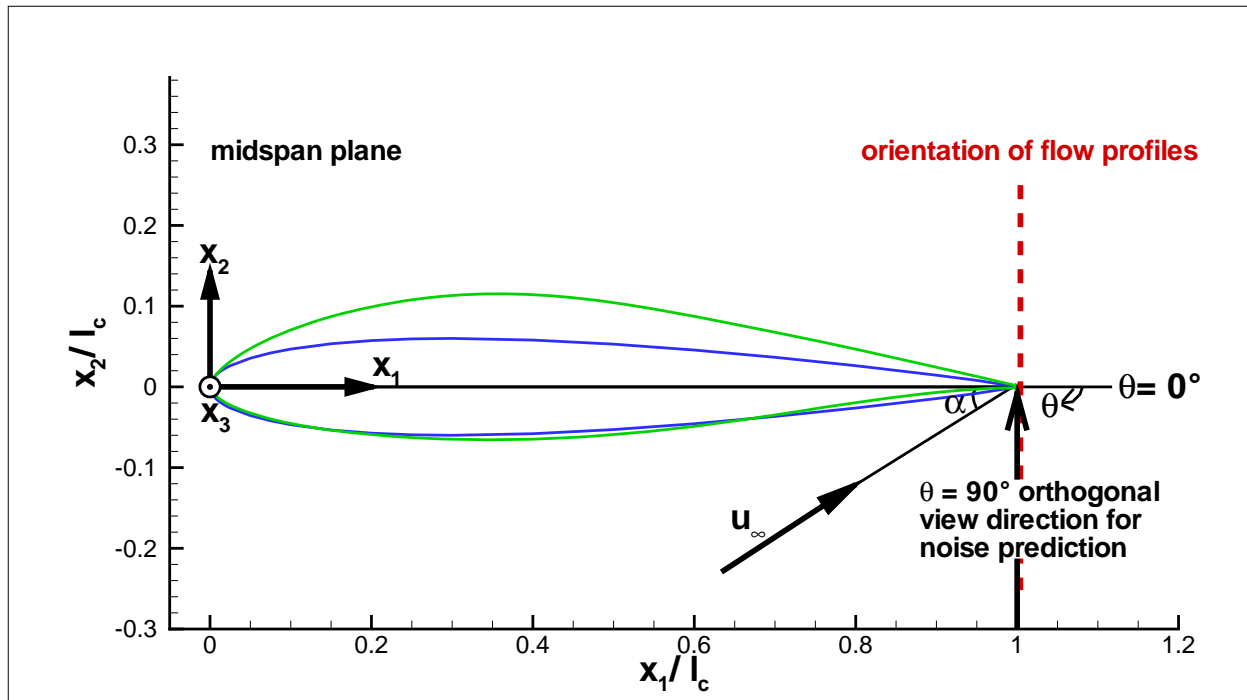

Figure 1. Coordinate system and parameter definition.

of available data sets including checks for satisfactory quality of the acoustic data. Moreover, the underlying well-documented measurement chains and model hardware have been recently used[23,40] and are still available for follow-on tests (for BANC-IV, etc.).[a] The test cases #1 to #4 have been mainly defined based on the availability of measured turbulence length scales and measured transition locations for these conditions,[23,29,30] while corresponding TEN and surface pressure data have been made available by scaling of multiple available data sets according to the problem statement. Case #5 for which no detailed flow survey is available corresponds to the original acoustic measurement conditions.[40] Airfoil profile coordinates were provided with zero thickness TE geometries, and zero inflow turbulence intensity should be considered for all cases[b]. Acoustic simulation results should refer to an observation distance of $r = 1$ m and a wetted span of $b = 1$ m.

It is understood that time accurate simulations of the unsteady flow field may be limited to a considerably shorter spanwise domain, e.g. combined with application of periodic boundary conditions. However, to allow a common baseline for comparison between different sets of results, participants were requested to correspondingly scale up their acoustic predictions. The choice of a suitable procedure was left to the

---

[a]Unfortunately, the hardware related to the extensive NASA data sets documented in Refs. 7, 8 has not been stored.

[b]Zero TE thickness and zero inflow turbulence intensity are defined herein because the current problem statement concentrates on pure broadband TBL-TE interaction noise; other relevant airfoil noise generation mechanisms like narrow band / tonal blunt TE vortex-shedding noise or turbulent-inflow leading-edge noise are correspondingly excluded. Tonal laminar vortex-shedding noise as well as flow separation / deep stall noise are avoided by transition forcing and by moderate angle-of-attack settings.

Table 1. Simulation matrix (order according to priority if computational resources are a limitation for the method; case #1 = single core test case for those submitters who could not afford to work on the full matrix).

#	airfoil	l_c, m	trans. position x_1/l_c	U_∞, m/s M_∞, - Re, -	T_∞, K ρ_∞, kg/m^3 p_∞, Pa	α, °	available comparison data
1	NACA0012	0.4	SS: 0.065 PS: 0.065	56.0 0.1664 1.50×10^6	281.5 1.181 95429	0	$L_{p(1/3)}$ $(\theta = 90°)$, G_{pp}, c_p, flow profiles at SS
2	NACA0012	0.4	SS: 0.065 PS: 0.065	54.8 0.1641 1.50×10^6	278.0 1.190 94975	4	$L_{p(1/3)}$ $(\theta = 90°)$, G_{pp}, c_p, flow profiles at SS
3	NACA0012	0.4	SS: 0.060 PS: 0.070	53.0 0.1597 1.50×10^6	273.8 1.224 96188	6	$L_{p(1/3)}$ $(\theta = 90°)$, G_{pp}, c_p, flow profiles at SS
4	NACA0012	0.4	SS: 0.065 PS: 0.065	37.7 0.1118 1.00×10^6	283.1 1.171 95156	0	$L_{p(1/3)}$ $(\theta = 90°)$, G_{pp}, flow profiles at SS
5	DU96-W-180	0.3	SS: 0.12 PS: 0.15	60.0 0.1730 1.13×10^6	299.3 1.164 100004	4	$L_{p(1/3)}$ $(\theta = 90°)$

participants; at minimum a scaling according to $p_{rms}{}^2 \propto b/r^2$ should be applied. For the TBL development and hence, TEN generation it is important that the measured transition locations x_1/l_c in table 1 are reproduced in the simulations[c]. The choice of how transition forcing is realized was also left to the participants. Exact tripping geometries and positions during the experiments are provided for optional use in the full version of the problem statement.[21] Therein, the interested reader will also find a more specified definition of simulation parameters and supplementing formatting details of the requested simulation data. Overall, participants were requested to calculate the following relevant acoustic and aerodynamic quantities:

- farfield one-third-octave band TEN spectra in terms of $L_{p(1/3)}(f_c)$, referenced to $r = 1$ m, $b = 1$ m, $\theta = 90°$, and corresponding directivities;

- unsteady surface pressure (point) power spectral density (PSD) $G_{pp}(f)$ at both the suction side (SS) and pressure side (PS) of the airfoil at 99 % l_c;

- chordwise distributions of the static surface pressure coefficient c_p and wall friction coefficient c_f;

- chord-normal profiles of the normalized mean flow velocity U_1/U_∞, normal Reynolds stresses $\langle u_1{}^2 \rangle/U_\infty^2$, $\langle u_2{}^2 \rangle/U_\infty^2$, $\langle u_3{}^2 \rangle/U_\infty^2$ (if available), and kinetic energy of turbulence k_T/U_∞^2 in the near wake at 100.38 % l_c;

- similarly, chord-normal distributions of the isotropic turbulence mean dissipation rate ϵ and longitudinal integral length scale Λ at 100.38 % l_c.

- integral 'boundary-layer' parameters, derived from the near-wake mean flow profiles at 100.38 % l_c, e. g. the BL displacement thickness δ_1 or momentum loss thickness δ_2.

Experimental comparison data from multiple facilities are available for identical or slightly different test conditions for the cases indicated in table 1. Individual data sets and applied scaling procedures to

---

[c]Effective transition positions x_1/l_c were measured by means of a stethoscope; these are taken as the position where the boundary layer (BL) was fully turbulent; i. e. intermittency regions extend between the leading edge of the tripping device and x_1/l_c.

compensate for present deviations from the idealized simulation conditions are surveyed in the BANC-II-1 documentation.[21,22]

III.   Overview of BANC-III-1 contributions

Contributions were submitted by (i) the Politecnico di Torino (PoliTo), Department of Mechanical and Aerospace Engineering (DIMEAS), Italy, in cooperation with Metacomp Technologies, Inc. and wavePRO S.R.L., (ii) the DLR Institute of Aerodynamics and Flow Technology, Braunschweig, Germany, (iii) the Institute of Aerodynamics & Gas Dynamics (IAG) at University of Stuttgart, Germany, and (iv) DTU Wind Energy, Technical University of Denmark (DTU), Roskilde. The corresponding authors and their respective contributions are summarized in table 2. DLR and IAG already participated in the BANC-II workshop, whereas PoliTo and DTU were new contributors.

Table 2. Overview of BANC-III-1 contributions (for complete definitions of abbreviations cf. p. 3 or the text below).

institution	authors	used computational approach	delivered prediction data
PoliTo	A. Iob[a] R. Arina P. Batten[b] S. Chakravarthy[b]	hybrid RANS/LES (IDDES) coupled with synthetic turbulence LEST (Large-Eddy STimulation) and FWH farfield propagation (RANS: CFD^{++} + SA, QCR terms)	c_p, c_f distributions, near-wake characteristics, $L_{p(1/3)}(f_c)$ at $\theta = 90°$ and directivities for case #1 only
DLR	C. Rautmann R. Ewert	CAA solver PIANO, coupled with stochastic source model FRPM (Fast Random Particle-Mesh Method), based on RANS statistics (RANS: TAU + SST)	c_p, c_f distributions, near-wake characteristics (full matrix), G_{pp} at PS and SS, $L_{p(1/3)}(f_c)$ at $\theta = 90°$ and directivities for cases #1–5
IAG	M. Kamruzzaman D. Bekiropoulos	simplified theoretical surface pressure model (Blake-TNO-derivative) Rnoise (RANS-based TE noise prediction model) with farfield propagation according to Brooks & Hodgson,[7] based on diffraction theory^{9,10,24} (RANS: FLOWer + SST)	c_p, c_f distributions, near-wake characteristics (full matrix), G_{pp} at PS and SS, $L_{p(1/3)}(f_c)$ at $\theta = 90°$ (no directivities) for cases #1–5
DTU	F. Bertagnolio	simplified theoretical surface pressure model (Blake-TNO-derivative), with farfield propagation according to Brooks & Hodgson,[7] based on diffraction theory^{9,10,24} (RANS: EllipSys2D + SST)	c_p, c_f distributions, near-wake characteristics (full matrix), G_{pp} at PS and SS, $L_{p(1/3)}(f_c)$ at $\theta = 90°$ (no directivities) for cases #1–5

[a]wavePRO S.R.L., Torino, Italy
[b]Metacomp. Technologies Inc., Agoura Hills, CA, USA

American Institute of Aeronautics and Astronautics

III.A. Used computational approaches

This section contains a brief description of the used methods and computational setup specifications, high-lighting the differences compared to BANC-II-1. All applied methods have been developed in an industrial context, i.e. with the objective to use broadband TEN prediction capability in the framework of low-noise airfoil design processes. It is therefore intended to balance prediction accuracy and universality vs. efficiency. In preparation of the workshop the participants were asked to summarize the particularities of their used approaches in a 'one-slide-presentation'. These schematic overviews are documented in figures 2 to 4.

III.A.1. PoliTo approach: non-zonal hybrid RANS/LES (IDDES) coupled with synthetic turbulence LEST and FWH farfield propagation

Broadband TEN prediction techniques based on Large-Eddy Simulation (LES), for the evaluation of noise sources, and on an acoustic analogy, for the computation of the acoustic radiation, have proven accurate and reliable. However, the high computational cost of LES prevents its widespread application as an aeroacoustics design and optimization tool. To include broadband noise prediction in the industrial design chain less computationally intensive procedures are required.

To this end, hybrid RANS/LES methods have been gaining in popularity. By employing a thin layer of near-wall RANS modeling, these methods make it possible to economically and accurately predict separated flow at comparatively high Reynolds numbers. Substantial difficulties still remain in translating turbulence energy from RANS statistics into the LES data contents.[4] To bridge this gap, the present work considers the use of a synthetic turbulence model, the so-called Large-Eddy STimulation (LEST) which allows to automatically convert the statistics provided by RANS closures into fluctuating turbulent velocity fields that are suitable for sustaining an embedded LES.

Here, LEST is coupled with the Improved, Delayed Detached-Eddy Simulation (IDDES) approach of Shur et al.[41] as an alternative framework for partially resolving and partially modeling the relevant aeroacoustic sources. IDDES extends the application area of (D)DES to mixed flow cases with both attached and separated regions by permitting the activation of RANS and LES modes in different flow regimes.

Fine, sub-grid-scale turbulence motions are modeled through a stochastic reconstruction that uses the statistics obtained from IDDES with additional quadratic constitutive relations (QCR) to generate an approximately realizable set of Reynolds stresses.[3] Noise radiated from the resolved larger-scale structures is propagated through a limited numerical sub-domain as far as a set of porous data-capture surfaces that are subsequently used as input to a separate Ffowcs-Williams and Hawkings (FWH) solver to propagate the signal to an arbitrary farfield observer point.
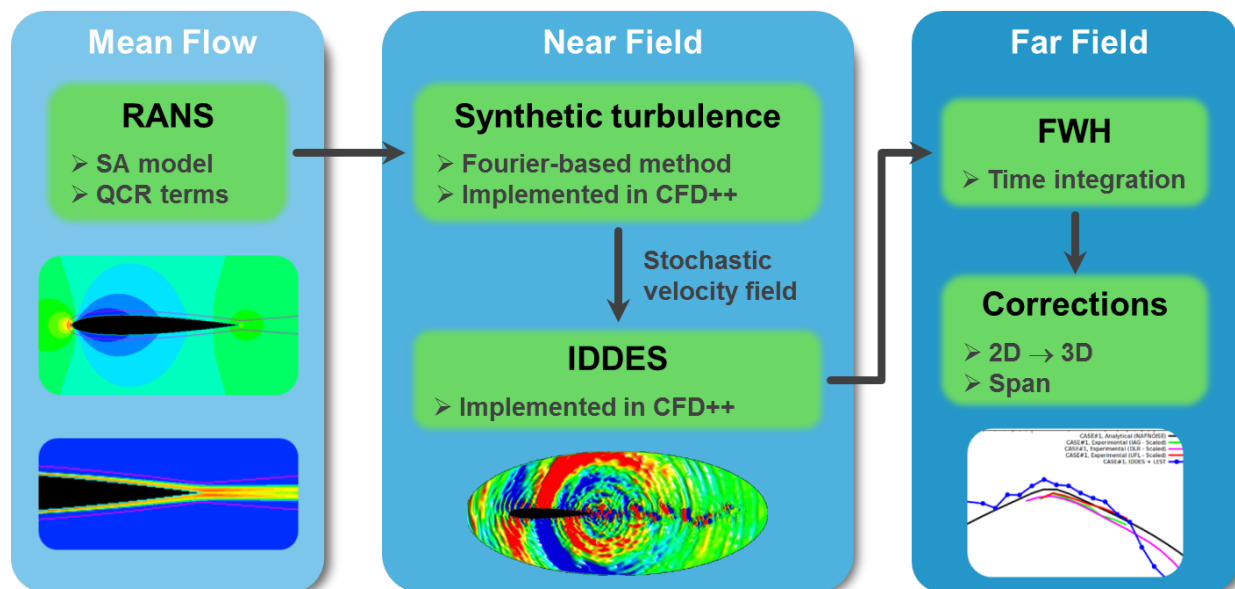

Figure 2. Schematic overview of PoliTo approach.

RANS computational setup: The rectangular domain for the initial 2D RANS calculation was set up to extend $7.5\,l_c$ from the leading edge of the airfoil in both the upstream and vertical directions and $17.5\,l_c$ in the downstream direction from its TE. The domain was discretized using an overset composite grid method; an airfoil body-fitted mesh was imposed on a Cartesian background grid. The airfoil grid was constructed using a C-type topology. The grid clustering off the walls was selected such that the first interior cell is located at $y^+ < 1$ to allow a solve-to-wall solution. The background mesh is uniform near the airfoil with a cell size of about 1 mm and then gradually coarsens towards the outer boundaries. Initial flow fields were obtained through steady-state RANS calculations using the Spalart-Allmaras (SA) turbulence model, augmented with QCR terms. Free-stream conditions were imposed at the outer boundaries and a no-slip condition was employed on the surface of the airfoil. Absorbing farfield layers were imposed at the outer boundary by the introduction of a source term of the form $K(U - U_\infty)$, where K is an automatically tuned damping coefficient, U is the solution vector and U_∞ corresponds to the farfield data used to define the boundary condition. The inlet flow field was laminar and the BL was tripped by introducing a virtual trip wire, which acts as a local source for the turbulence equations. The tripping sources simulate a trip wire of radius 1 mm located on the airfoil at $x_1 = 0.05\,l_c$ on both the SS and the PS.

IDDES computational setup: To reduce the computational time and the errors related to the propagation of the acoustic waves, the region of the IDDES mesh was kept as small as possible. The RANS domain is therefore reduced to an elliptic sub-domain surrounding the airfoil, as shown in figure 2 (bottom center). IDDES technically requires a full 3D solution to account for spanwise fluctuations. However, initial computations here were made in 2D to first ascertain that the synthetic turbulence would be able to sustain the unsteadiness in the airfoil wake which is otherwise not self-initiating in such weakly unstable flows. These 2D results were submitted to BANC-III-1 and corrected for 3D effects,[17,26] whereas 3D computations (with a 0.1 m span) have been accomplished after the submission date.

Even in these 2D simulations, errors in the BL profile are expected to be small, since the majority of the airfoil BL is maintained in RANS mode. Furthermore, although sound waves should be propagating and therefore, attenuating spherically, it is possible to introduce corrections to account for the decorrelations which should occur in a 3D span and to correct for the cylindrical nature of the acoustic wave spread on a 2D mesh. The IDDES domain was isolated by cutting out the initial RANS mesh in the elliptic region around the airfoil. Therefore, the acoustic calculation used the same overset composite grid, i.e. a C-type topology grid for the body-fitted mesh around the airfoil and a uniform background mesh. Even though the outer boundary of the IDDES domain is very close to the airfoil, no spurious reflections were evident. The 3D version of the mesh was obtained by extruding in the span. This approach allows the initial RANS solution to be mapped directly onto the acoustics mesh with no interpolation errors.

For a complete documentation of the PoliTo contribution the interested reader might additionally refer to Iob et al.[26]

III.A.2. DLR approach: CAA code PIANO with RANS-based stochastic source model FRPM

A hybrid CAA approach with stochastic source model has been applied by DLR. The general outline of the approach used for the BANC-III computations corresponds to that of BANC-II, refer to the BANC-II-1 documentation[22] for additional details given there. Further improvements of the method used for BANC-III comprise the effective realization of more general turbulence spectra of, e.g., Liepmann or von Kármán type that exhibit a roll-off in the inertial sub-range with constant power law exponent (Liepmann: $n = -6/3$, von Kármán: $n = -5/3$) instead of the rapid roll-off of Gaussian spectra realized before. A brief description of the approach with additional references is given below.

As an overview, figure 3 presents a flowchart of the hybrid two-step procedure. In a first step the turbulent flow around the airfoil is derived from steady RANS simulation[d]. For BANC-III the two-equation Menter-SST turbulence model[32] is used, for details refer to Rautmann et al.[38] A CAA simulation is carried out in the second step solving Acoustic Perturbation Equations (APE[14]) on a structured multi-block (SMB) mesh. RANS flow provides the mean-flow for the time-dependent aeroacoustic simulation and the turbulence statistics to synthesize stochastic vortex sound sources that drive the governing equations. The accurate reconstruction of fluctuating sound sources based on local inhomogeneous turbulence statistics is realized with the 'Fast Random Particle-Mesh Method' (FRPM).[16,18] The 'Random Particle-Mesh Method' (RPM) was introduced in 2005.[19] FRPM was proposed in 2007[15] as an improved numerical version with further

---

[d] The CFD simulations were performed with the DLR TAU code in version 2014.1.0.
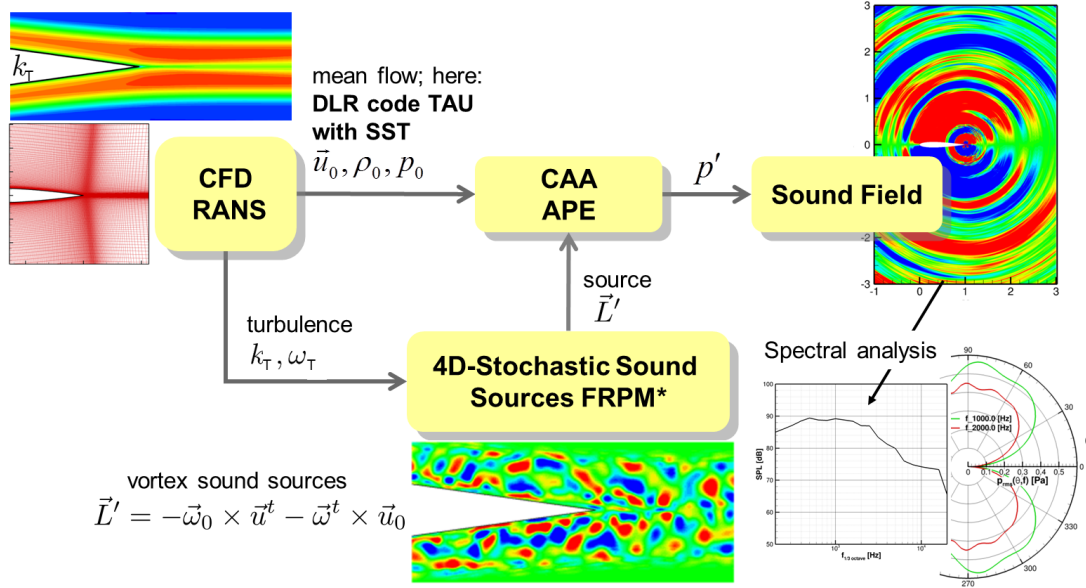
Figure 3. Schematic of hybrid RANS-based CAA prediction method by DLR.

increased efficiency. The main building blocks of FRPM are:

1. Creation of a solenoidal (divergence free) field of fluctuations by superposition of model vortices of random strength and spatial shape (blob) function derived from Gaussian distribution; the vortices advect in a prescribed non-uniform mean-flow field.

2. Efficient numerical realization of the superposition of vortices via random particles and efficient recursive 1D Gaussian filters applied on an auxiliary FRPM mesh (source patch).

FRPM has been applied for 2D and 3D CAA problems. Mathematically, a fluctuating 3D solenoidal velocity field is created by the superposition of P random vortex particles,

$$u'_i = \epsilon_{ijk} \frac{\partial}{\partial x_j} \sum_{p=1}^{P} G(\boldsymbol{x} - \boldsymbol{x}_p, \Lambda) \hat{A}(\boldsymbol{x}_p)\, r^n_{pk}(\boldsymbol{x}_p), \tag{1}$$

where u'_i is the i-th component of the fluctuating synthesized velocity vector of dimension 3 at a discrete time level n (dependence on n not explicitly indicated). The resulting velocity field is strictly divergence free (solenoidal), i.e. $\partial u'_i / \partial x_i \equiv 0$. The summation with index p runs over all random particles. The random particles are represented by their positions $\boldsymbol{x}_p$ and carry 3 Gaussian random variables r^n_{pk} per particle. Here, p indicates the particle number, and k indicates the random variables, which are Gaussians with vanishing mean, $\left\langle r^n_{pk} \right\rangle = 0$, and mutually uncorrelated between different particle ($p \neq q$) and different variables ($k \neq l$), having a variance defined by $\left\langle r^n_{pk} r^n_{ql}(t) \right\rangle = \delta_{pq}\delta_{kl}\rho_p^{-1}$, where ρ_p is the local particle density of the particle cloud at the particle position. The particles passively advect in the local RANS mean-flow, i.e. $\dot{\boldsymbol{x}}_p = \boldsymbol{u}_0$. The particle seeding and distribution is realized for the low Mach-number BANC-III TEN cases so that a constant particle density is obtained and maintained throughout each simulation. For BANC-III frozen turbulence is realized, i.e.[e] $r^{n+1}_{pk} = r^n_{pk}$. For frozen turbulence the entire source term from Eq. (1) is differentiable in space and time and thus poses no problem when combined with standard CAA discretization techniques. The shape function $G(\boldsymbol{x} - \boldsymbol{x}', \Lambda)$ defines the realized model vortex associated to each particle. For FRPM a Gaussian distribution with standard deviation proportional to the turbulent integral length scale Λ is selected as a shape function. The vorticity distribution around the particle position (vortex blob function)

---

[e]Decaying turbulence with specific decay time can be realized by defining the random variable by means of an Ornstein-Uhlenbeck process (Langevin equation) with according time scale.

American Institute of Aeronautics and Astronautics

is defined by the Laplacian of the shape function, $\nabla^2 G$ ('Mexican hat'). The function $\hat{A}$ specifies the actual local variance realized by the fluctuations. In 3D it scales as $\hat{A} = \sqrt{2\rho_0 k_T/3\pi\Lambda}$, where ρ_0 is the RANS mean density. More details about the scaling can be found in Refs. [16],[18]. In this way an energy spectrum of Gaussian shape and integral length scale Λ is realized. The integral length scale is derived from RANS using a calibration constant $c_l \simeq 0.5$, hence $\Lambda = c_l/C_\mu \sqrt{k_T}/\omega_T$ ($C_\mu = 0.09$). It was shown in Refs. [16],[20] that the outlined procedure generates isotropic turbulence. An extension to anisotropic turbulence will be proposed in Ref. [39].

For the numerical evaluation of Eq. (1) a direct simple computation of the shape function $G\left(\boldsymbol{x} - \boldsymbol{x}', \Lambda\right)$ in the surroundings of each particle locations $\boldsymbol{x}_p$ is avoided due to its numerical inefficiency. Rather, the random variates of each particle are projected via trilinear interpolation from the particle to an auxiliary background mesh (denoted as 'source patch') that defines the resolved source area. The Gaussian is evaluated on the source patch via successive application of 1-D Gaussian filtering in each coordinate direction.[18] The typical speed-up for the evaluation of Eq. (1) yields 2 orders of magnitude compared to simple evaluation. Furthermore, Gaussian filtering can be realized with optimized signal processing algorithms, e. g. those proposed by Young & van Vliet[46] (constant length scale) or that of Purser[36],[37],[42] (variable length scale). Application of the Young & van Vliet recursive Gaussian filter to the previous example yields a further speed up reaching a three orders of magnitude saving in computational time compared to simple evaluation of the sum.

FRPM improvement: Previous TEN simulations have shown that the spectrum has a too steep decrease in the higher frequency ranges compared to experimental data. It was supposed that this too early drop-off is caused by the underlying Gaussian spectrum provided by FRPM. Therefore, an extension of FRPM has been applied that allows the realization of more general turbulence spectral. The extension to other turbulence spectra by means of an adapted shape function in Eq. (1) has been proposed e. g. by Dieste.[13] The extended filter functions of more elaborated turbulence spectra usually are not separable so that the sum in Eq. (1) must be directly evaluated. In recent work an efficient extension of the Gaussian based FRPM method to more complex turbulence spectra of Liepmann[38] or von Kármán type[45] are realized by a superposition of mutually uncorrelated Gaussian spectra of different length scales. The length scale is constant for each realization, which allows for application of the efficient Young & van Vliet filter. The derivation of more complex spectra is derived analytically by means of Gaussian transformation proposed by Alecu et al.,[2] refer to Refs. [38],[45]. With 5 to 10 superposed Gaussian an excellent realization of more complex spectra is obtained. For the BANC-III simulations a Liepmann spectrum has been used. All Gaussian spectra are generated with N mutually uncorrelated FRPM realizations. Different constant length scales l are used for each realization, ranging from the minimum non-dimensional length scale l_{min} to the maximum length scale l_{max}. Between l_{min} and l_{max} N steps with length scale increment $\Delta l = (l_{max} - l_{min})/N$ are defined[f]. The minimum length scale l_{min} depends on the resolution of the computational grid in the source area. The turbulence kinetic energy to be used for each realization is defined for the Liepmann spectrum by[38]

$$k_{T_{mod}}(l) = k_T \frac{2\Delta l}{\pi\Lambda} \exp\left(-\frac{l^2}{\Lambda^2\pi}\right).$$
(2)

CAA computational setup: The CAA solver PIANO[12] (Perturbation Investigation of Aerodynamic NOise) of DLR is used, which is based on the 4th order accurate DRP scheme proposed by Tam & Webb.[44] The simulations are carried out generating one turbulent 2D 'slice' out of the 3D turbulent field (refer to Ref. [17]) and conducting a CAA simulation on a 2D mesh. It was shown in Ref. [17] that a 2D-to-3D correction has to be applied to the spectrum to correct the 2D simulation for 3D sound radiation. The correction does not reveal explicit frequency dependence. Therefore, a constant level off-set results, which has been removed for the BANC-III simulation by determining once a calibration off-set via comparison with CASE #1 experimental data. Acoustic perturbation equations are solved on a two-dimensional computational domain extending about 6 by 6 chord-lengths with the airfoil in the center. A structured multi-block mesh is selected to utilize the parallelized computation with PIANO. This grid consists of 64 blocks with a total number of 1.1 million cells. The mesh is smoothed across the block boundaries. A 800 by 200 cells FRPM source patch with the dimension $x_1/l_c = 0.4$ by $x_2/l_c = 0.1$ centered at the TE is used. The computation of the acoustic source term from RANS and FRPM data is sketched in figure 3 and discussed in Ref. [22]. A wall clock time of less than 20 hours for one simulation is realized with the prescribed approach for parallel computation on 16 CPUs.

---

[f]For BANC-III a linear distribution is selected, in other cases an exponential spacing appeared more suitable.[45]

III.A.3.   IAG approach: RANS-based TE noise prediction model Rnoise

IAG's Rnoise is a fast simplified theoretical TEN prediction method that combines a prediction of the unsteady surface pressure wavenumber frequency spectrum $P(k_1, k_3, \omega)$ at the TE with a simple farfield noise prediction based on diffraction theory. The same approach was already applied to produce BANC-II-1 results[22] and only minor changes to the included modeling where introduced herein.

The main modeling effort lies accordingly in the prediction of $P(k_1, k_3, \omega)$ that is generally calculated as solution of a simplified Poisson equation.[6, 27, 29, 35] Rnoise incorporates a derivative of the frequently applied prediction schemes based on Blake's[6] approach, herein referred to as 'Blake-TNO' models because the most widespread (mainly in the context of low-noise wind turbine profile design efforts) is the variant published by Parchen,[35] TNO. The general Blake-TNO approach reads

$$P(k_1, k_3, \omega) = 4\rho_\infty^2 \left(\frac{k_1^2}{k_1^2 + k_3^2} \right) \int_0^\infty \left[\frac{\mathrm{d}U_1(x_2)}{\mathrm{d}x_2} \right]^2 \Lambda_2(x_2)\, \tilde{\Phi}_{22}(k_1, k_3; x_2)\, \langle u_2^2(x_2) \rangle\, \Phi_m(\omega - k_1 U_c) \exp^{-2|k||x_2|}\, \mathrm{d}x_2. \tag{3}$$

Once $P(k_1, k_3, \omega)$ is known TBL-TE farfield noise can be calculated by representing the surface pressure fluctuations as a distribution of harmonic evanescent waves. Solving the diffraction problem,[9, 10, 24, 25] combined with the specific test conditions and corresponding model simplifications in the experiment of Brooks & Hodgson,[7] corresponding to the present problem definition ($\theta = \phi = \pi/2$ and $\beta = 0$), leads to the following applied farfield solution:

$$S_{ff}(\omega) = \frac{b}{4\pi r^2} \int_{-\infty}^\infty \frac{\omega}{c_\infty k_1} P(k_1, 0, \omega)\, \mathrm{d}k_1. \tag{4}$$

In Eq. (3) $\Lambda_2(x_2)$ is the wall-normal integral length scale of the turbulence field and $\tilde{\Phi}_{22}(k_1, k_3; x_2)$ the (anisotropic) two-dimensional wavenumber spectrum of the normal velocity fluctuations u_2 that has been normalized with the wall-normal Reynolds stress component, i. e. $\tilde{\Phi}_{22}(k_1, k_3; x_2) = \frac{\Phi_{22}(k_1, k_3; x_2)}{\langle u_2^2(x_2) \rangle}$.

$\Phi_m(\omega - k_1 U_c)$ is the so called 'moving-axis' spectrum describing the temporal evolution of the eddies during their passage of the TE, i. e. the effects of generation and decay of turbulence on $P(k_1, k_3, \omega)$. U_c denotes the convection velocity of the turbulent structures within the TBL.

To complete the prediction scheme additional models must be formulated for these quantities. While the mean velocity gradient $\mathrm{d}U_1(x_2)/\mathrm{d}x_2$ can be directly extracted from the RANS solution, the quantities $\Lambda_2(x_2)$, $\langle u_2^2(x_2) \rangle$, $\tilde{\Phi}_{22}(k_1, k_3; x_2)$, and $\Phi_m(\omega - k_1 U_c)$ depend on the respective turbulence model applied. For details of the correspondingly used formulations the interested reader might refer to Kamruzzaman.[27]
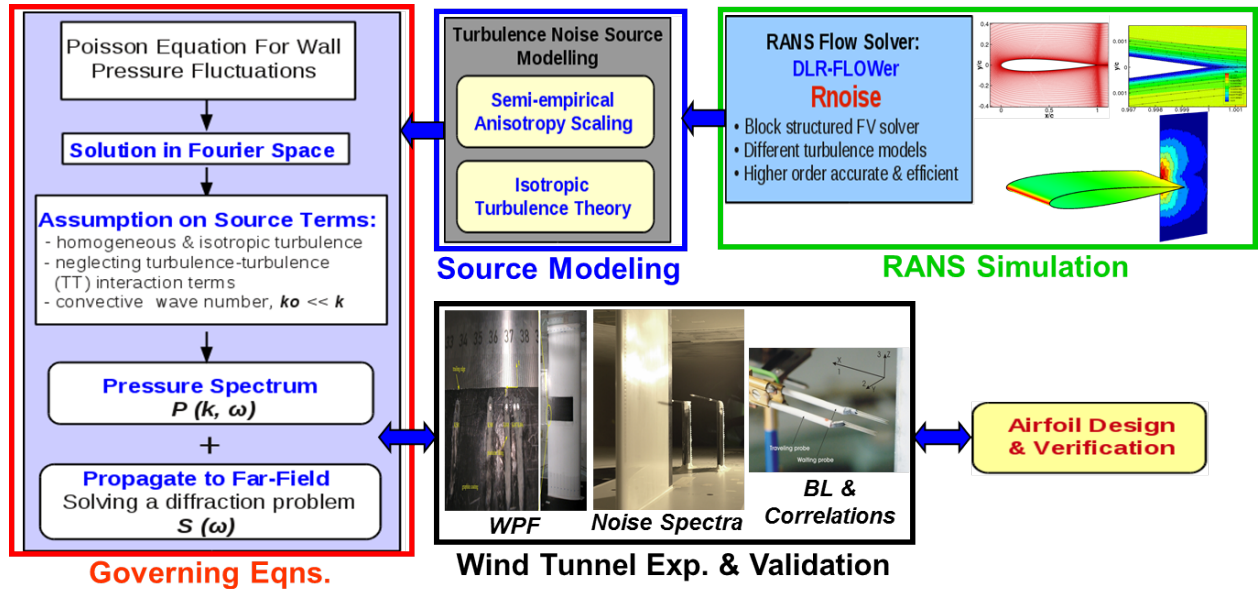

Figure 4. Schematic overview Rnoise by IAG.

RANS computational setup: The necessary flow quantities are extracted from a RANS CFD calculation. Principally, the noise calculation in Rnoise can be selectively based on different anisotropic or isotropic turbulence models while in the latter case anisotropic effects are correspondingly corrected for by use of semi-empirical scaling functions. The herein presented RANS results have been produced by means of the DLR code FLOWer, applying the Menter SST two-equation turbulence model.[32] Details of the applied anisotropy correction and supplementing modifications of the original dissipation model equation can be found in the work of Kamruzzaman.[27] A cell-centered finite-volume formulation on block-structured grids is utilized for the computations presented here. A C-type structured mesh consisting of $672 \times 128 = 86016$ cells in streamwise and airfoil-normal direction is used for the simulations. The y^+-value is assumed to be 1 in the first layer above the surface of the airfoil in all computations, providing a sufficient resolution with more than 30 cells across the BL. All CFD simulations from BANC-II-1 were repeated based on renewed computational grids.

Rnoise improvement: Compared to previous simulations for the BANC-II-1 workshop new models for the moving axis spectrum $\phi_m(\omega - k_1 U_c)$ and the convection velocity of turbulent eddies U_c were introduced.[28] In the previous version of the Rnoise code, the same model for the moving axis spectrum as applied by DTU was used, i.e. Eq. (7) below, assuming $U_c = 0.7 U_\infty$. In Eq. (7) α_2 describes the spread of the Gaussian distribution of the function, hence representing a time scale which accounts for the non-frozen turbulence. Here, an alternative integral time scale Θ_2 is introduced to replace α_2 in the updated Rnoise version, i.e.

$$\phi_m(\omega - k_1 U_c) = \frac{\Theta_2}{\sqrt{\pi}} \exp[-(\omega - k_1 U_c)^2 \Theta_2{}^2], \text{ where } \Theta_2 = \frac{\Lambda_2}{\sqrt{\langle u_2^2 \rangle}}. \tag{5}$$

The new time scale Θ_2 can be modeled directly from CFD data and therefore, the former dependency on the empirical constant in the denominator $(0.035 U_\infty)$ is removed. For the calculation of the convection velocity, the standard equation $U_c = 0.7 U_\infty$ is replaced by the following empirical expression which is based on the mean flow velocity U_1 and the BL thickness δ:

$$\frac{U_c}{U_\infty} = 0.92 - \frac{1}{8} \ln(k_1 \delta), \text{ where } k_1 = \frac{\omega}{U_1}. \tag{6}$$

With this approach, the convection velocity ranges from $0.55 U_\infty$ and $0.9 U_\infty$.

III.A.4. DTU approach: RANS-based simplified theoretical surface pressure model combined with Brooks & Hodgson's farfield noise prediction based on diffraction theory (i.e. Chandiramani, Chase, Howe)

Similar to the method applied by IAG, the DTU method relies on a surface pressure prediction of Blake-TNO-type. A comprehensive description of the procedure has been previously published by Bertagnolio et al.[5] The main results are reminded below. A formula similar to Eq. (3) is used to model the surface pressure. The major differences with the IAG approach are the following:

1. The equation is multiplied by a factor 2 as a consequence of the assumed symmetry of the two-points correlation function of the vertical velocity fluctuations at any point along the normal to the wall when looking toward or away from the wall.

2. The anisotropy of the spectrum $\tilde{\Phi}_{22}(k_1, k_3; x_2)$ is related to stretching factors which are driven by the mean pressure gradient near the TE.

3. The correlation length scale $\Lambda_2(x_2)$ is defined as function of frequency (in addition to its x_2-dependency) and of the anisotropy stretching factors following the derivation proposed by Lynch et al.[31]

4. Herein, the moving-axis spectrum is modeled using the original TNO approach[35] which consists of a Gaussian distribution as

$$\Phi_m(\omega - k_1 U_c) = \frac{\alpha_2}{\sqrt{\pi}} \exp[-(\omega - k_1 U_c)^2 \alpha_2^2], \text{ where } \alpha_2 = \frac{\Lambda_2}{0.05 U_c} \tag{7}$$

and $U_c = 0.7 U_1$ (being here related to the local mean flow velocity, not to U_∞). However, note that little differences were observed when using a Dirac function instead.

In the same way as in the IAG approach, Eq. (4) is used to evaluate the farfield noise.

RANS computational setup: The input values for the model across the TBL are obtained from the in-house 2D Navier-Stokes incompressible solver EllipSys. The equations are discretized by means of a finite volume formulation. It uses a cell-centered grid arrangement for the pressure field and the Cartesian velocity components and the velocity-pressure decoupling is circumvented by using the classical Rhie and Chow interpolation technique. The numerical code requires that the computational domain must be mapped onto a boundary-fitted structured grid. In order to reduce computational time, a domain decomposition technique has been implemented and the software is run on a parallel CPU platform. Details about the numerical code and discretization issues can be found in Refs. 33, 34, 43.

In the present calculations, a steady state solution is sought in the form of the RANS equations. A second-order upwind scheme is applied to compute the convective fluxes whereas viscous terms are discretized using the classical second-order central difference scheme. The two-equation SST turbulence model by Menter[32] in its original version is used to obtain the turbulent viscosity. The O-type meshes used for these calculations are refined near the airfoil surface so that the non-dimensionalized distance of the first mesh point from the airfoil surface always satisfies the condition $y^+ \leq 1$ as required for this type of computations. All grids used for 2D RANS calculations extend 35 chords away from the airfoil. They contain 256 cells around the airfoil and 256 from the airfoil to the outer boundary. In accordance with the original TNO model,[35] the turbulent normal stress is here assumed proportional to the turbulence kinetic energy as

$$\langle u_2^2(x_2) \rangle = c_k k_T(x_2), \tag{8}$$

where the empirical constants are set to $c_k = 0.45$ on the SS, and $c_k = 0.3$ on the PS, respectively.

In contrast to previous simulations with the present model,[5] BANC-III-1 test cases involve the implementation of tripping devices for transition forcing. To account for the tripping devices used in the measurements, the transition location in the calculations is fixed. To this end, a standard γ-Re_θ transition model is used and the tuning factor $\gamma = 4$ for the intermittency is locally applied in the transition region. The factor γ basically drives the amount of energy injected in the BL during transition. However, the exact handling of specified trip tapes represents a longer-term effort being subject to future BANC contributions. As it will be observed later, a consequence of this technique is the appearance of large friction coefficient values in the region where the transition is enforced and this may be considered as a local numerical artifact.

It should also be noted that, in deviation from the BANC-III-1 problem statement, the TBL profiles were here extracted at $x_1/l_c = 99$ % and not at $x_1/l_c = 1.0038$ %.

IV. Results

IV.A. Comparison of c_p- and c_f-distributions

Figures 5 and 6 present the predicted c_p- and c_f-distributions for cases #1–3 and #5. Available comparison data (here: measurement data and/or XFOIL predictions) are plotted in black color and delivered prediction data in red (PoliTo), green (DLR), magenta (IAG), and blue (DTU). This color coding will be kept throughout the following code-to-code comparisons of results.
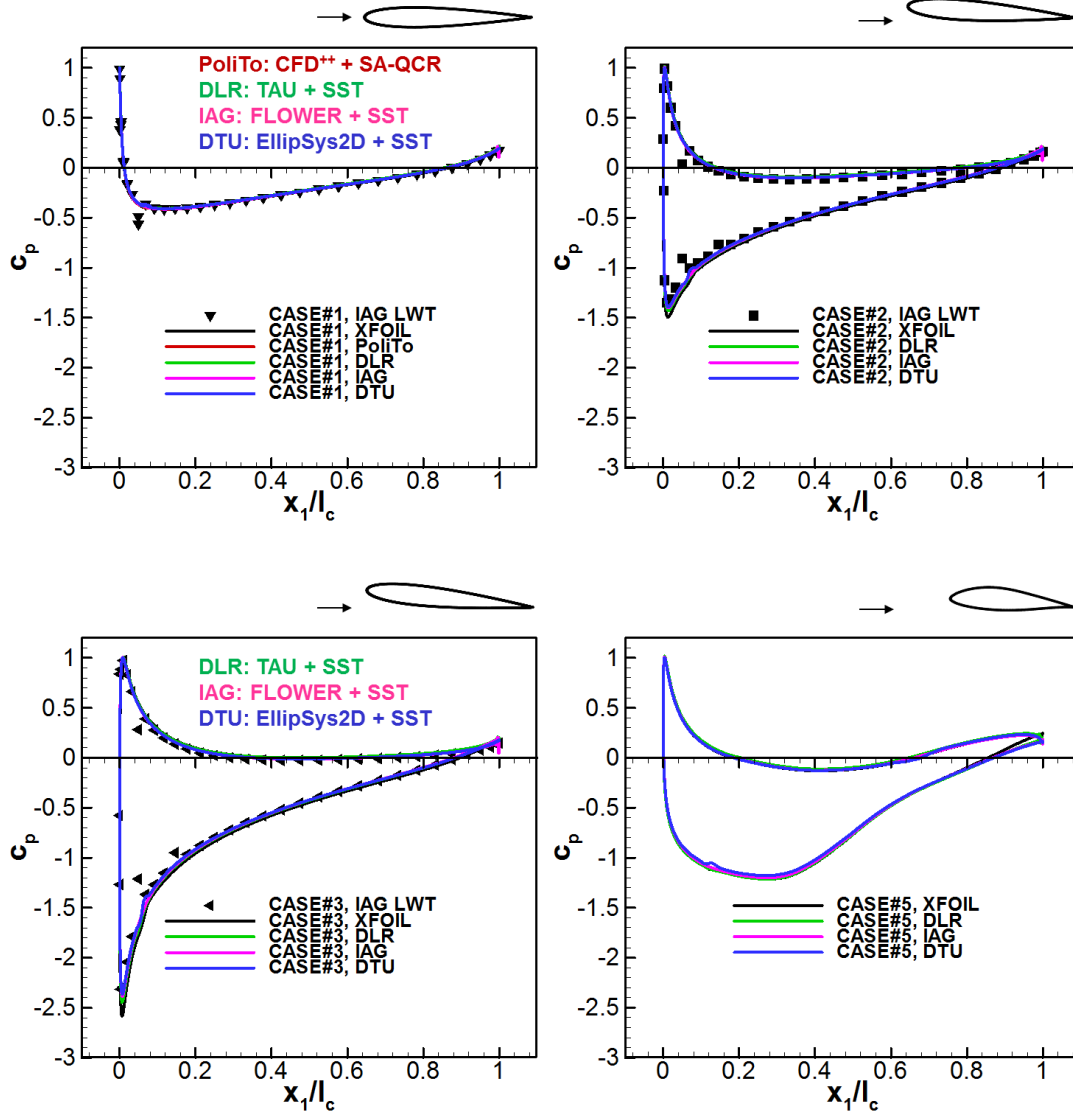

Figure 5. Distributions of static pressure coefficients c_p for cases #1–3 and #5 (case #4 equivalent to case #1 and therefore omitted). Experimental validation data originate from measurements from IAG's Laminar Wind-Tunnel (LWT).

American Institute of Aeronautics and Astronautics

According to figure 5 predicted c_p-distributions delivered by PoliTo, DLR, IAG and DTU lie on top of each other. The available measurement data sets for cases #1–4 are well reproduced except for positions close to $x_1/l_c = 0.05$ where application of the tripping devices disturbed the measurement.

Differences between the c_f-predictions in figure 6 can be observed in the area of the nominal transition locations (see table 1). While PoliTo, DLR and IAG predictions are quantitatively similar for cases #1–4, DTU predictions provide dominating c_f peaks at $x_1/l_c \approx 0.06$–0.07 (cases #1–4, SS and PS) or $x_1/l_c \approx 0.12$ (case #5, SS only), respectively. These can be explained by the particular setting of the intermittency factor in the transition model (cf. section III.A.4, p. 13). Different to BANC-II-1[22] larger deviations between DLR and IAG predictions for case #5 are documented with significantly lower c_f values in the IAG results. Except for the DTU prediction for case #5, where the TBL transition on the PS occurs much farer downstream, the nominal transition locations are generally well captured in all simulations.
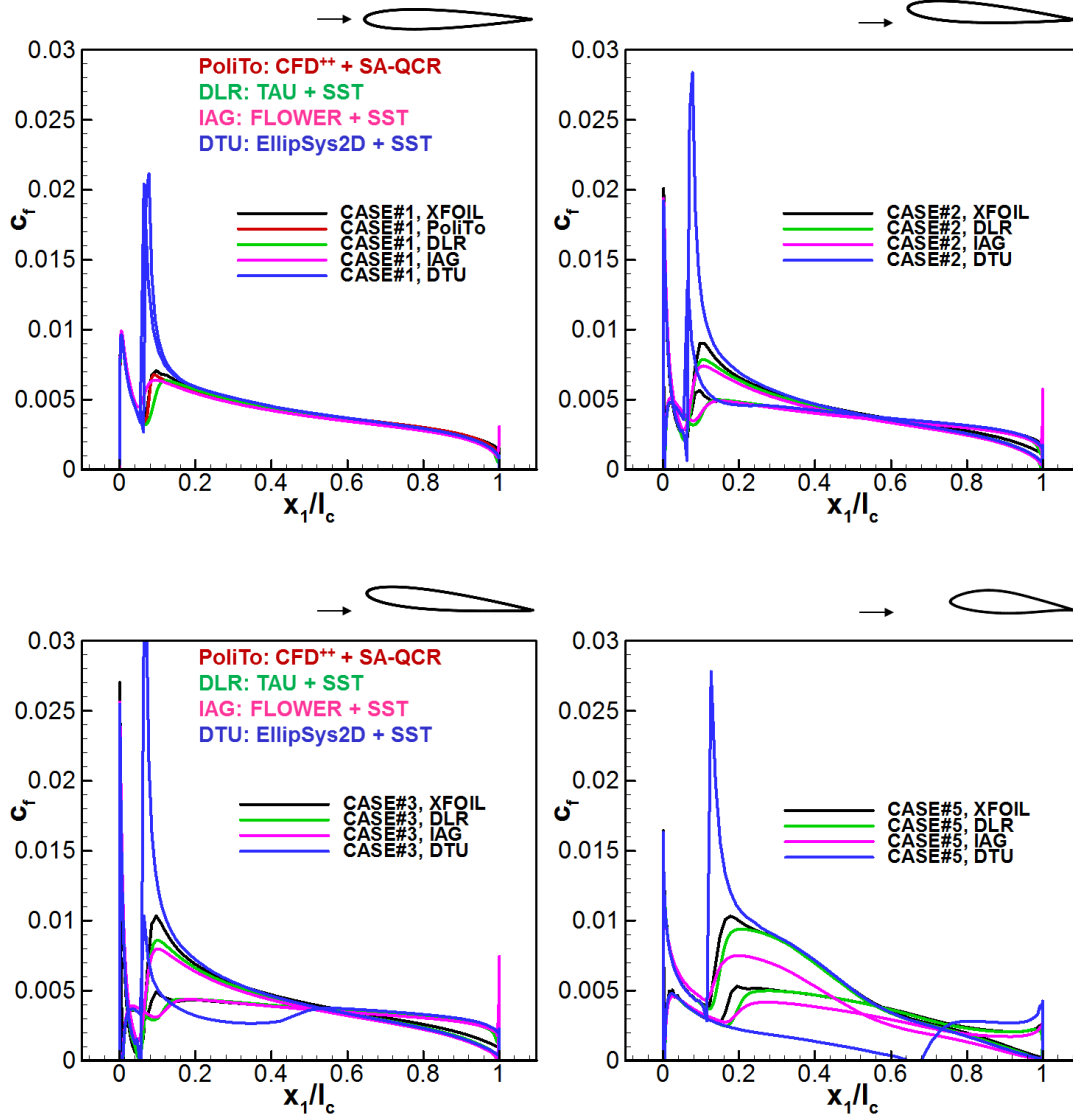
Figure 6. Distributions of wall friction coefficients c_f for cases #1–3 and #5 (case #4 equivalent to case #1 and therefore omitted), only code-to-code comparisons, since c_f has not been measured.

American Institute of Aeronautics and Astronautics

IV.B. Comparison of near wake flow characteristics

Table 3 summarizes the derived integral TBL thicknesses from both measurements and simulations. Experimental validation data originate from measurements in the Laminar Wind-Tunnel (LWT) at IAG. As it was already stated in Ref. 22, differences between measured and predicted values of δ_1 and δ_2 seem to rather reflect deviant procedures to determine these values. Overall, the corresponding near-wake profiles from which these integral thicknesses were derived, are better suitable for code-to-code comparisons.
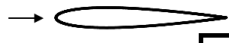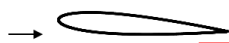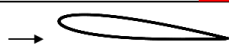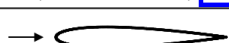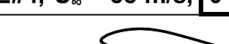
A detailed survey of the extracted mean flow profiles and corresponding profiles of the turbulence characteristics at $100.38\,\%\,l_c$ is provided in the following figures 7 to 11. As shown therein, the near-wake U_1 profiles are well predicted by all CFD approaches. In particular for the symmetric TBL test cases #1 and #4 an almost perfect reconstruction of the velocity profiles is documented.

In accordance to the observations during BANC-II-1, the normal Reynolds stresses and k_T are also best predicted for cases #1 and #4, whereas prediction quality decreases (with the general tendency of underpredicting the measured values) for the non-symmetric TBL cases. Results provided by PoliTo (case #1 only) slightly overpredict k_T. Contrary to the predictions by IAG, DLR and DTU, the corresponding normal Reynolds stresses display a fairly weak level of anisotropy, but are still in reasonable agreement with the measurement data.

Note that the shown DLR and DTU predictions rely on conventional assumptions of the normal stress ratio used along with the predicted k_T value, when applying the two-equation Menter SST model.[32] DLR predictions were derived based on the relationships $\langle u_3^2 \rangle = 2/3\,k_T$ and $\langle u_1^2 \rangle : \langle u_2^2 \rangle : \langle u_3^2 \rangle = 4 : 2 : 3$. For the Blake-TNO approaches (viz. IAG and DTU) at least the correct reproduction of $\langle u_2^2(x_2) \rangle$ is required. Therefore, DTU provides estimates for this component only; Eq. (8) reads $\langle u_2^2 \rangle = 0.45\,k_T$ for the SS which is almost identical to $\langle u_2^2 \rangle = 4/9\,k_T$ in the DLR estimate. It is worth to note that these straightforward approaches based on commonly used empirical factors lead to almost perfect prediction results for $\langle u_2^2(x_2) \rangle$.

Previously, in the framework of the forerunner BANC-II-1 workshop,[22] DLR applied the Reynolds stress turbulence model (RSM). Corresponding directly predicted $\langle u_1^2 \rangle$, $\langle u_2^2 \rangle$ and $\langle u_3^2 \rangle$ are repeated here (dashed green lines) for cases #1–4 to demonstrate the relatively small differences compared to the current more pragmatic procedure.[g]

Table 3. Survey on integral TBL properties (PoliTo transition positions in brackets denote trip wire positions in the simulations).

PoliTo (red) — DLR (green) — IAG (pink) — DTU (blue)

	TRANSITION START SS / PS	δ_1, mm SS / PS	δ_2, mm SS / PS	δ_1, mm SS / PS	δ_2, mm SS / PS
CASE#1, U_∞ = 56 m/s, 0°	[5.0% / 5.0%]	as measured (IAG):		2.8 / 2.8	1.7 / 1.7
	6.5% / 6.5%			2.5 / 2.5	1.5 / 1.5
	6.5% / 6.5%	3.0 / -	1.7 / -	2.5 / 2.5	1.4 / 1.4
	6.5% / 6.5%			2.7 / 2.7	1.6 / 1.6
CASE#2, U_∞ = 55 m/s, 4°	6.5% / 6.5%			3.7 / 1.9	2.0 / 1.2
	6.5% / 6.5%	4.8 / -	2.3 / -	3.8 / 1.7	1.9 / 1.0
	6.5% / 6.5%			4.0 / 1.8	2.2 / 1.2
CASE#3, U_∞ = 53 m/s, 6°	6.0% / 7.0%			4.5 / 1.6	2.3 / 1.0
	6.0% / 7.0%	5.7 / -	2.5 / -	6.7 / 1.4	3.8 / 0.9
	6.0% / 7.0%			5.0 / 1.3	2.5 / 0.9
CASE#4, U_∞ = 38 m/s, 0°	6.5% / 6.5%			2.8 / 2.8	1.6 / 1.6
	6.5% / 6.5%	3.1 / -	1.8 / -	2.8 / 2.8	1.5 / 1.5
	6.5% / 6.5%			2.9 / 2.9	1.7 / 1.7
CASE#5, U_∞ = 60 m/s, 4°	12.0% / 15.0%			5.0 / 1.2	2.0 / 0.8
	12.0% / 15.0%	- / -	- / -	6.1 / 1.1	2.4 / 0.7
	12.0% / 67.0%			5.6 / 0.6	2.2 / 0.4

---

[g]It has to be recalled that anisotropic turbulence realization in FRPM has not yet been included in BANC-III-1, i. e. the selection of higher level, more elaborate turbulence models beyond the minimum requirement (two-equation model) has no influence on TEN prediction results as long as a good prediction quality of k_T can be maintained. As described in section III.A.2 the reconstruction of source terms relies on k_T, whereas individual Reynolds stresses are not yet processed.
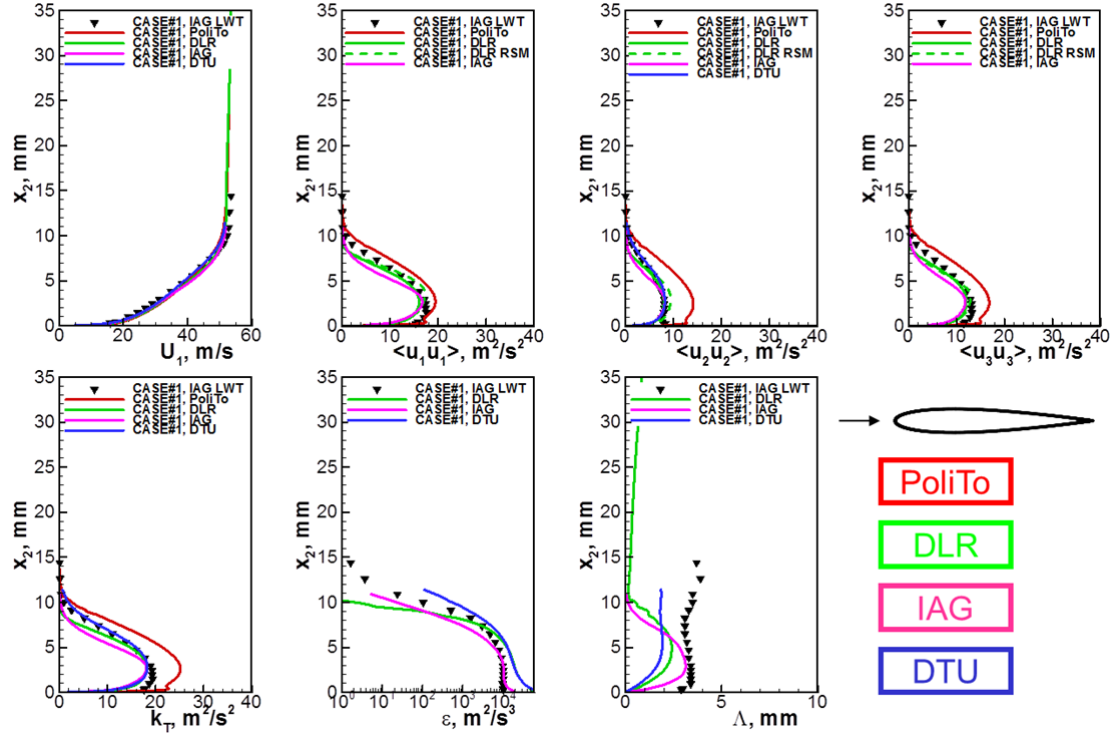
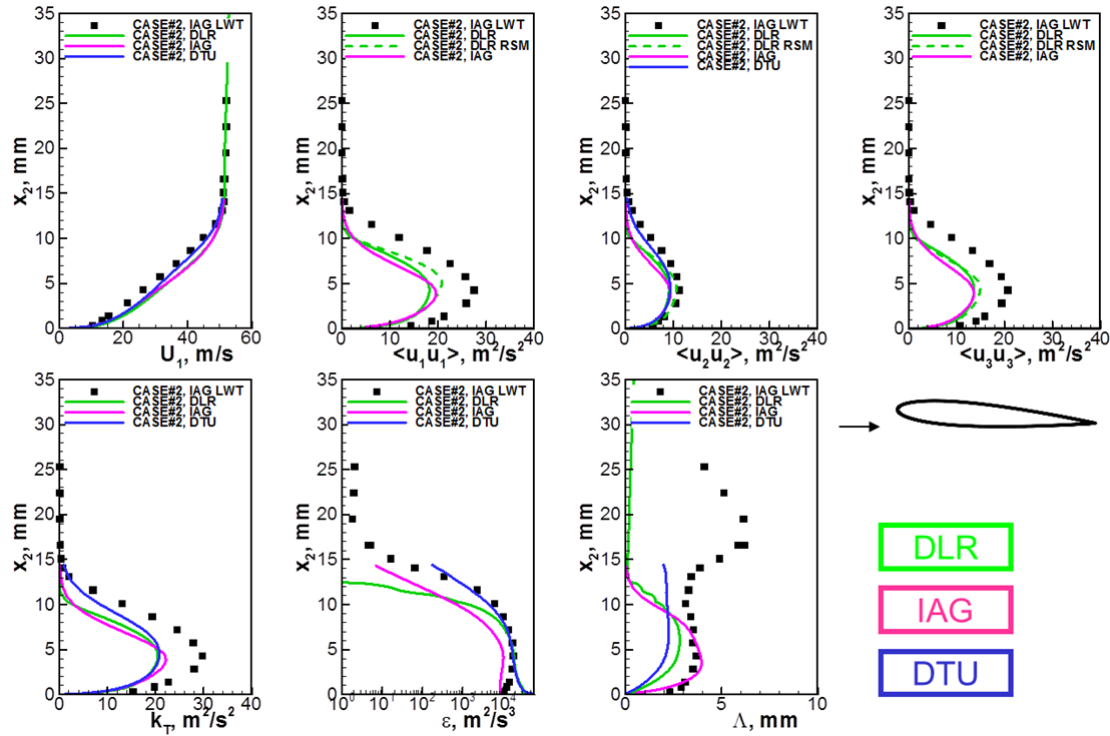Figure 7. Near-wake flow characteristics for case #1 (SS).

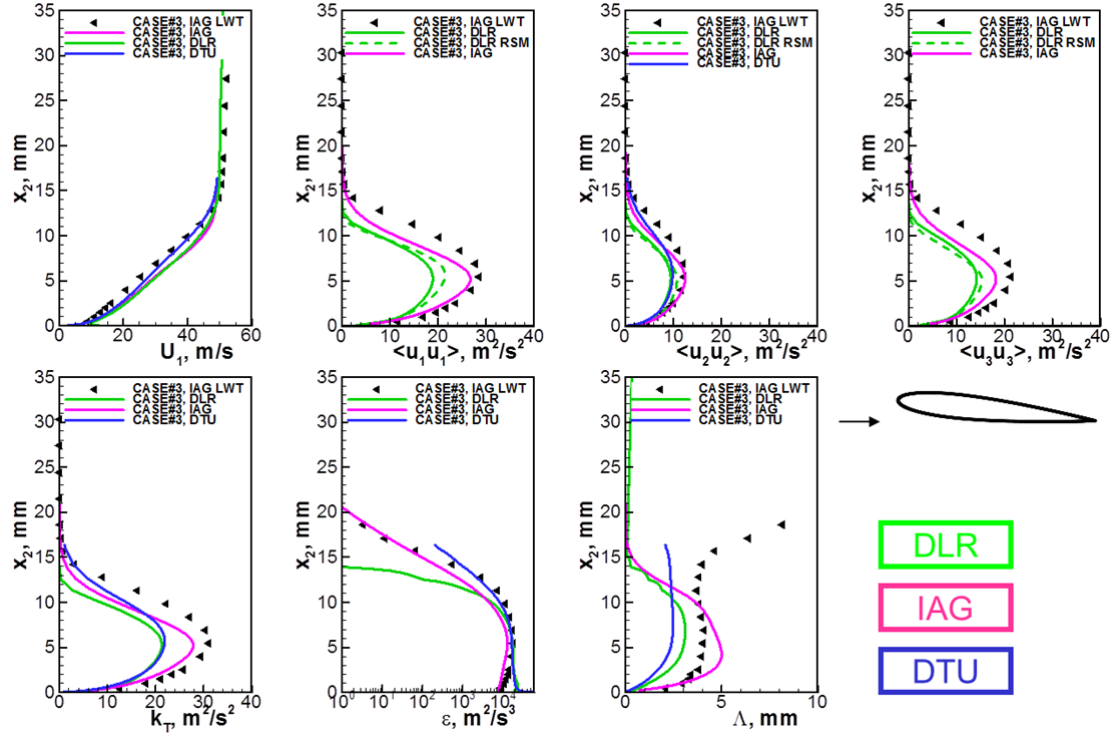Figure 8. Near-wake flow characteristics for case #2 (SS).

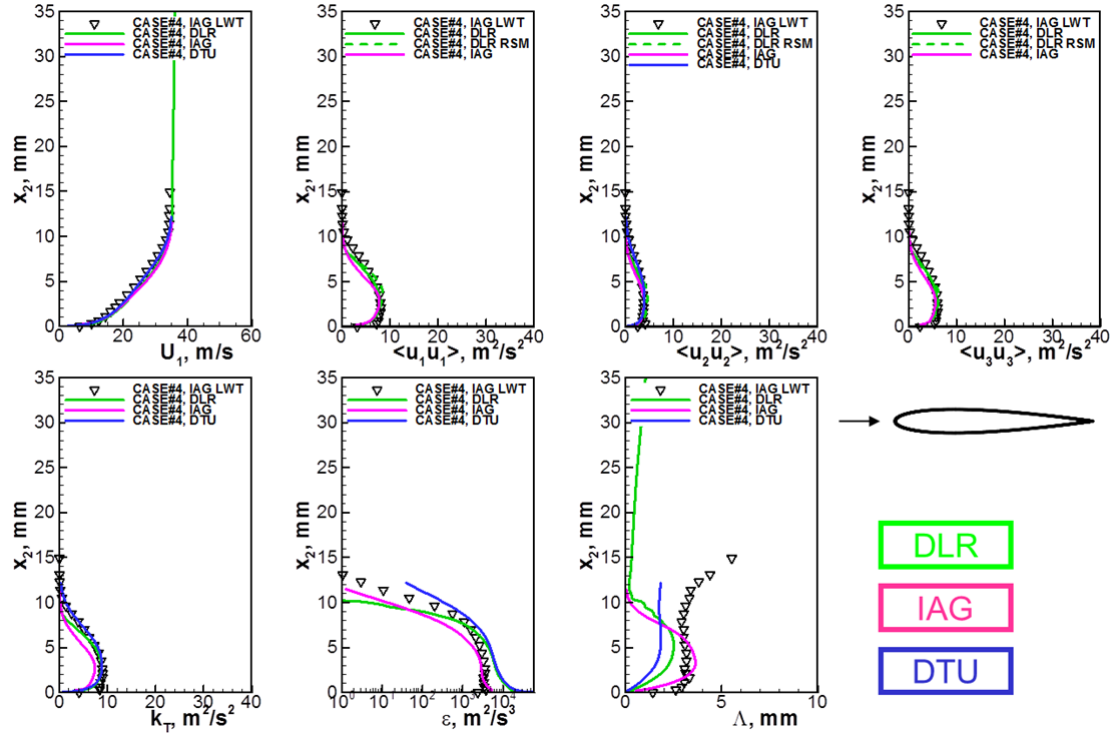Figure 9. Near-wake flow characteristics for case #3 (SS).

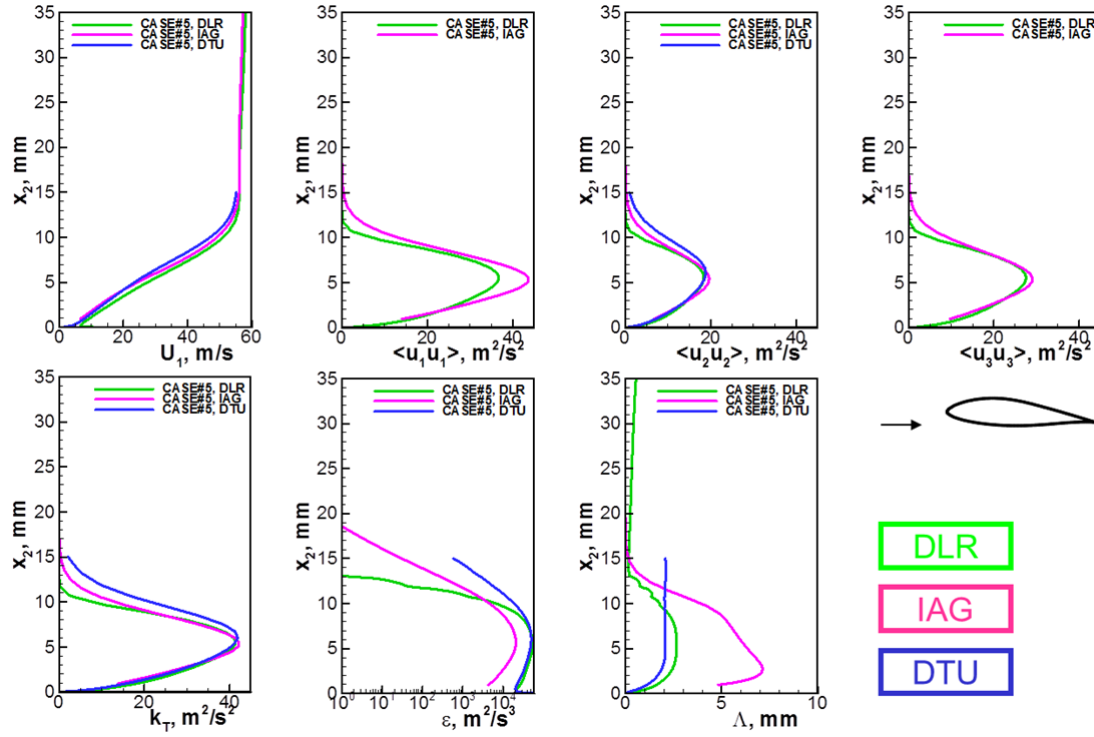Figure 10. Near-wake flow characteristics for case #4 (SS).

Figure 11. Near-wake flow characteristics for case #5 (SS), no experimental validation data available.

Finally, predictions for ϵ and Λ by DLR, IAG and DTU are compared to equivalently post-processed measurement data.[27,29,30] Corresponding predictions are not included in the PoliTo results because the applied SA-QCR turbulence model does not provide these values. For the ϵ profiles similar observations can be made as during BANC-II-1; when approaching the wall, ϵ is generally overpredicted by DLR and DTU (the latter providing overall larger values than the two other approaches), whereas the IAG method contains a dedicated near-wall correction. Note that the resulting more realistic ϵ values in close proximity to the wall lead also to larger isotropic integral length scales Λ in the IAG results. Derivation of Λ follows directly from k_T and ω_T or ϵ, respectively.[h] The combination of k_T and ϵ in the IAG prediction leads to unphysical, non-zero values of Λ outside the BL. Therefore, a scaling function based on k_T was incorporated into the IAG calculation method. The scaling function mainly affects the outer part of the Λ distribution resulting in more realistic values and a decrease towards zero at the BL edge.

Compared to BANC-II-1,[22] the prediction quality of the IAG RANS results could be further improved; in particular, formerly observed overpredictions of the Λ maximum were reduced and for case #3 (figure 9) formerly underpredicted k_T (as well as corresponding normal Reynolds stresses) now display larger values close to the measured data. Note that an explanation for these improvements is simply given by a recalculation of the RANS matrix based on renewed computational grids. It has to be recalled that the model improvements presented in section III.A.3 have effectively no influence on the results shown here and exclusively affect the pressure prediction results. DLR and DTU approaches generally underpredict Λ which is partly the result of the described overprediction of the near-wall ϵ. Interestingly, measurement data rather indicate a constant Λ profile across wide portions of the TBL as it is observed also in the DTU predictions. To fit absolute values, however, the empirical constant c_l[h] would require a (case-dependent, i.e. variable) adjustment towards larger values.

---

[h]The details are e.g. provided above in section III.A.2, when describing the DLR approach: $\Lambda = c_l / C_\mu \sqrt{k_T} / \omega_T = c_l \, k_T^{3/2} / \epsilon$ ($C_\mu = 0.09$, $c_l \simeq 0.5$). Note that slightly different calibration constants were used among the BANC-III-1 participants, namely $c_l = (2/3)^{3/2} \approx 0.54$ by DLR, $c_l = 0.748 \, (2/3)^{3/2} \approx 0.4$ by IAG, and $c_l = 0.387$ by DTU. Post-processed measurement data follow the same relationship with $c_l = 0.4$.

IV.C. Comparison of surface pressure spectra

An overview of predicted and measured surface pressure PSDs close to the TE at $x_1/l_c = 0.99$ is provided in Figure 12, distinguishing between PSDs at the PS (dashed lines) and SS (solid lines) of the airfoil. The survey restricts to cases #1–3 and #5, while results for case #4 can be found below in section IV.E where the capability of predicting trends is evaluated.

Accordingly, PoliTo results overestimate the surface pressure levels at lower frequencies, whereas an underestimation is observed at higher frequencies. As a consequence, peak levels are predicted at too low frequencies when compared to the measurements. Possible reasons for these discrepancies are given below along with the interpretation of the corresponding farfield TEN prediction results. Similar observations are made for the low frequency contents of the PSDs provided by DTU; spectral peaks at both the PS and SS are overpredicted and located at too low frequencies. Contrary to that, the mid-to high frequency regions of
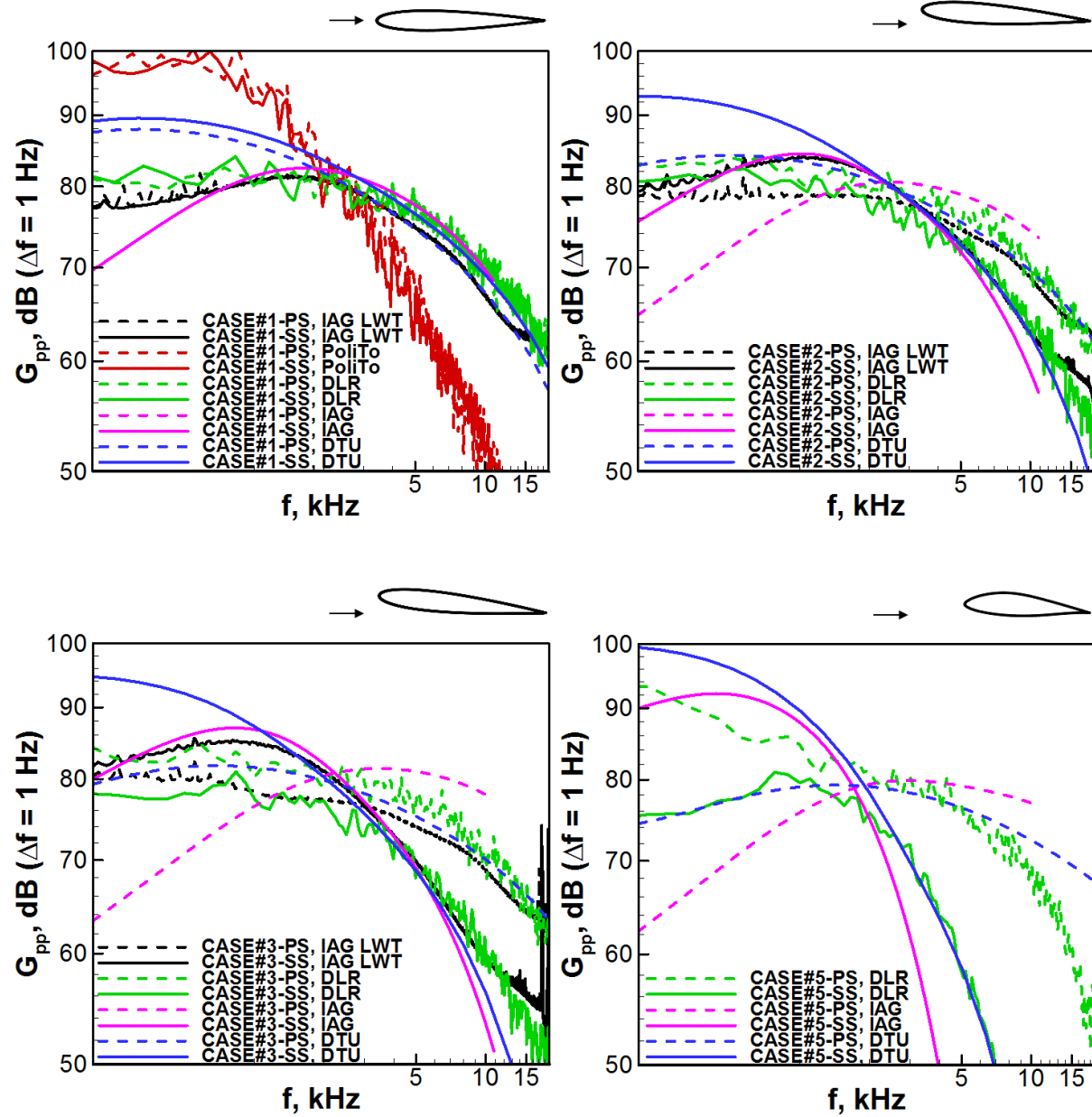

Figure 12. Unsteady surface pressure PSDs G_{pp} for cases #1–3 and #5. Experimental validation data originate from LWT measurements of IAG (no data available for case #5).

American Institute of Aeronautics and Astronautics

the PSDs are well reproduced in terms of level and spectral shape. A tentative explanation for the too large spectral values at lower frequencies predicted by the DTU approach is seen in the use of the von-Kármán-spectrum for the modeling of $\tilde{\Phi}_{22}(k_1, k_3; x_2)$. The latter does not accurately account for the presence of the airfoil surface, even if anisotropic stretching factors are applied. Thereby, the constraining effect on the sizes of the turbulent vortices, at least in the direction normal to the wall with possible redistribution of energy in the two other directions, is not properly modeled and may be responsible for the above discrepancies. However, studies of this aspect will have to be further developed to provide a definite clarification. The observed offset between the PS and SS surface pressure spectra for the symmetric cases #1 and #4 (cf. figure 18 below, p. 26) results from using different empirical factors for the derivation of $\langle u_2^2(x_2)\rangle$ on each side of the airfoil, see Eq. (8).

The variant Blake-TNO approach by IAG leads to more accurate predictions at the SS of the airfoil; spectral peak frequency and levels are well captured with only minor overestimates in levels. An exception is case #4 (figure 18) with much larger deviations from the measured PSD. Compared to BANC-II-1 results the introduction of the new models for ϕ_m and U_c have led to the anticipated improvement in the prediction of the peak frequency and the total amplitude,[22,28] i. e. the formerly larger overpredictions could be diminished by the suggested modifications. Nonetheless, for the PS a general overestimation of spectral peak levels and frequency is visible which is in parts more detrimental as previously observed during BANC-II-1. This behavior stems from a still inaccurate modeling of the TBL data on the PS. Indeed, for technically relevant cases (e. g. wind-turbine blades with loading) the major effort has to be set on a precise modeling of the SS contributions which mostly contribute to overall farfield TEN levels. It can be assumed, that an appropriate modeling of all necessary BL data will lead to a better reproduction of the measured spectra.

Different to the IAG and DTU approaches, the wall pressure spectra do not serve as a basis for the eventual calculation of farfield TEN spectra. Rather, the sound radiation is simulated directly as part of the CAA computation from the vortex dynamics in the vicinity of the TE as prescribed by stochastic modeling. The surface pressure spectra that result from 2D CAA simulation comprise hydrodynamic and acoustic pressure fluctuations at the wall with relative weighting different from that obtained from 3D CAA simulation. As a result, mainly hydrodynamic surface pressure spectra may be spoiled by additional acoustic contributions in the 2D CAA simulation. The spectral shape is correctly represented for cases #1 and #4, however, for the remaining cases predictions are reasonable at mid- to high frequencies only (here, they compare to the DTU results). At lower frequencies PS and SS contributions deviate from the measurements. 3D CAA computations are envisaged for BANC-IV that should enable proper realization of surface pressure spectra.

IV.D.   Comparison of acoustic farfield pressure spectra

Figure 13 provides an overview of the farfield TEN prediction results for cases #1–3 and #5. For case #4 refer to the discussion of the trend predictions in the following section.

Farfield TEN, referenced to a 1-m airfoil span, a 1-m observation distance, and a $\theta = 90°$ observation angle, is shown in a 1/3-octave band representation format of spectra. "Recommended comparison datasets"[21] (for details see figure 9 in Ref. 21) are herein averaged to condense available experimental data from different research groups and test facilities to one representative validation spectrum per test case. These averaged spectra, originating from measurements in IAG's LWT and DLR's Acoustic Wind-Tunnel Braunschweig (AWB), are highlighted in black color and provided with conservative ±3-dB error bars to account for systematic errors in the measurements (overall scatter observed among multiple-facility measurements at similar configurations[21]). Individual datasets contained in the BANC-II-1 data package are still displayed in their entirety but are reduced to greyscale to improve readability of the graphs.

The overall agreement between the shown predictions and experimental data is good for all test cases, given the comparatively large scatter band of the measurement data. Compared to BANC-II-1[22] the formerly observed large variation among predictions for case #5 could be significantly reduced. Nonetheless, prediction results from different approaches still feature their individual peculiarities.

Farfield TEN spectra provided by IAG and PoliTo roughly present the same tendencies observed for the surface pressure spectra: IAG results almost perfectly capture measured peak levels and frequencies (with the exception of case #4). Contrary to that, for the cases with higher aerodynamical loading (cases #3 and #5) the high frequency contents of the spectra is strongly overestimated. As it was concluded from the surface pressure results, the deviation is attributable to an inaccurate modeling of the relevant input parameters on the PS of the airfoil. PoliTo results show an overestimation of the peak level and an underestimation at
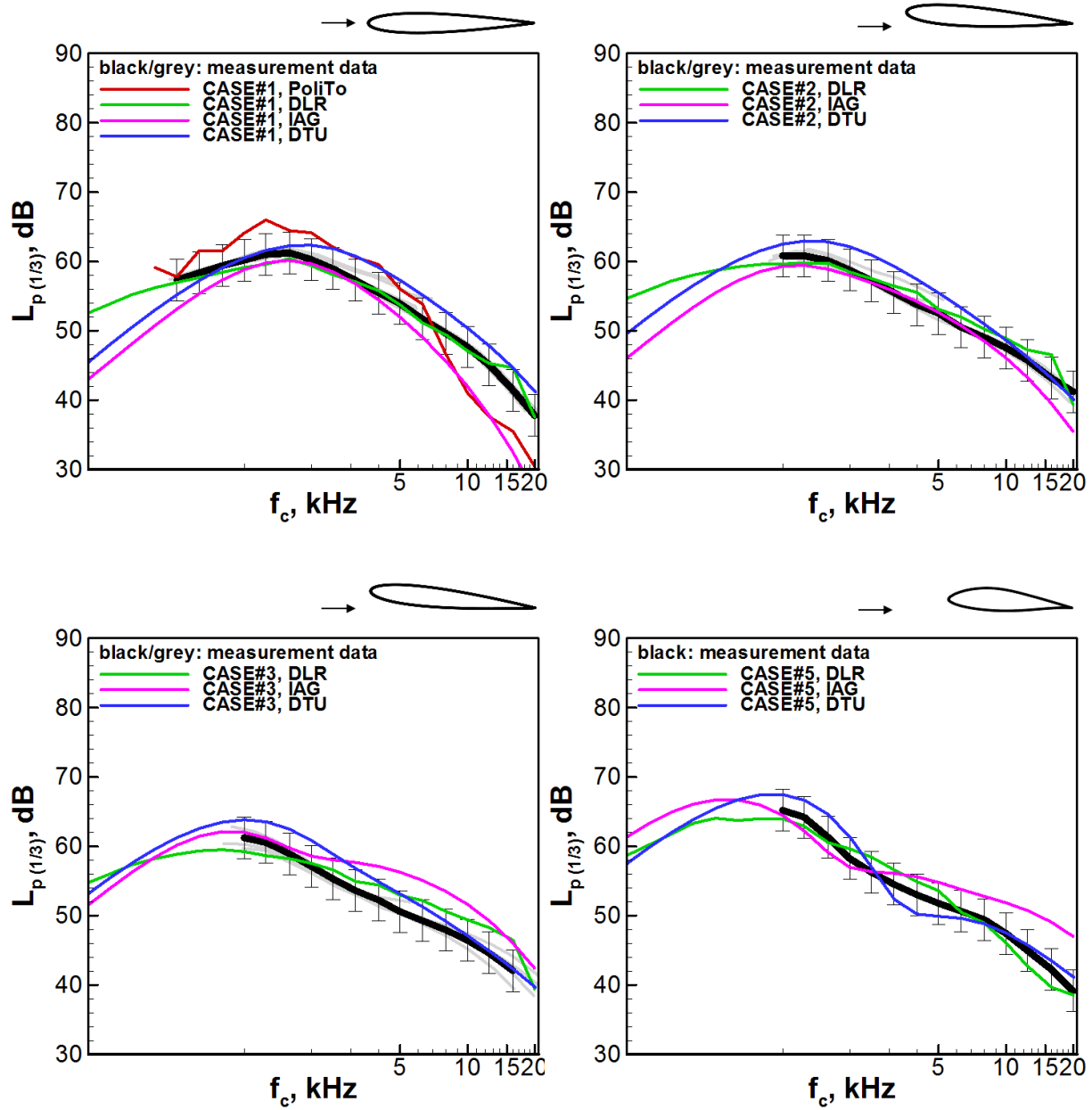
Figure 13. Overview of the achieved acoustic predictions compared to the measurement data. Experimental validation data from multiple facilities and research institutions, acquired with fundamentally different measurement techniques, are considered with a ±3-dB scatter band.

higher frequencies ($f_c > 8$ kHz). However, discrepancies appear less pronounced and the peak frequency is correctly predicted when compared to the surface pressure data. A possible explanation for the observed overpredictions is seen in a still imperfect conversion of RANS- into LES data contents. Induction of the synthetic turbulence, as it is divergence free in homogeneous turbulence only, could cause additional spurious noise. Since initial 3D computations indicate more substantial overprediction than observed here, at least the applied (partially empirical) 2D- to 3D correction can be excluded as a potential source of systematic error in the data post-processing.

Despite the observed discrepancies in the modeled surface pressure spectra, DTU farfield TEN results show a generally good agreement with the measured data. The significant overprediction of surface pressure spectra in this lower frequency region appears almost compensated in the farfield TEN prediction results. Predicted peak levels are rather located close to the upper limit of the given scatter band with the tendency towards higher frequencies than observed in the other prediction results. Particularly for cases #1 and #2 deviations occur compared to the measured peak frequencies. Note that prediction results for case #4 (figure 17, p. 26) are of excellent quality.

CAA results by DLR are located within the provided measurement scatter band over almost the full frequency range. Minor exceptions are observable only at high frequencies $f_c > 10$ kHz. Spectral peak levels and frequencies are in accordance with the measurements. For the cases with higher aerodynamical loading (case #3 and #5) peak levels are lower compared to DTU and IAG prediction results. For case #3 the maximum appears broader and less expressed.

Since for the majority of test cases farfield TEN measurement data are unavailable for frequencies $f_c < 1$ kHz, it remains unclear at these frequencies which of the predicted spectral shapes are closest to reality.

Finally, to illustrate the effect of the introduced modifications of the prediction approaches since BANC-II-1, a direct comparison of current and previous BANC-II-1 results of DLR and IAG is provided in figure 14. The most important results are as follows:

- The frequency range of DLR predictions was extended towards frequencies < 1 kHz lower than the measurement limit so that peak frequencies are now clearly identifiable and available for code-to-code comparisons. Moreover, DLR predictions for case #5 could be significantly improved due to corrections of simple errors identified in the data post-processing. Application of the Liepmann turbulence spectrum leads to the anticipated slope reduction in the mid- to high frequency spectral decay region beyond the peak. As a consequence, prediction quality for cases #1, 2, 4 (the latter not shown in the figure) and #5 was increased. Only for case #3 the slope appears overcompensated and the former BANC-II-1 result looks favorable.

- As mentioned above, IAG model improvements lead to almost perfect predictions of the SS peaks in the surface pressure spectra, whereas PS spectra remain overpredicted. The most distinctive consequences for the farfield TEN predictions are (i) the misprediction of the higher frequency range for case #3 which is not observable in the BANC-II-1 results, and (ii) a systematic adjustment of spectra in the lower frequency region for all test cases. Compared to BANC-II-1, peak levels are slightly reduced and shifted towards higher frequencies, thereby affecting the region of the low-frequency spectral roll-off. In this region the TEN prediction quality is moderately reduced for case #1 (compare in figure 12 also the corresponding shape deviations of the surface pressure spectra). Differences compared to BANC-II-1 might be additionally related to modifications in the used CFD input quantities.

1/3-octave band normalized[i] farfield TEN directivity patterns for $r = 1$ m are shown in figures 15 and 16 for center frequencies $f_c = 1$ kHz, $f_c = 2$ kHz, $f_c = 5$ kHz, $f_c = 8$ kHz, and $f_c = 10$ kHz. Mutual comparison is herein restricted to case #1 (figure 15) because only PoliTo and DLR provided directivity predictions. Fundamental differences between the predicted TEN directivities are observed. The principal shapes consisting of two predominantly forward-inclined main lobes (with increasing number of side lobes for growing f_c) as well as symmetric directivity patterns for $\alpha = 0°$ are according to expectation. In figure 16 also the rotation of the directivity patterns with increasing α is documented. It is hoped that future BANC-workshops based on an increased number of contributions will enable a more detailed assessment of the respective individual shapes and non-symmetries (the latter particularly observable for case #5).

---

[i]Directivities are displayed in terms of normalized rms sound pressures as $p_{rms}(\theta)/\overline{p_{rms}(\theta)}$ with $\overline{p_{rms}(\theta)} := \frac{1}{2\pi} \int_0^{2\pi} p_{rms}(\theta)\, \mathrm{d}\theta$.
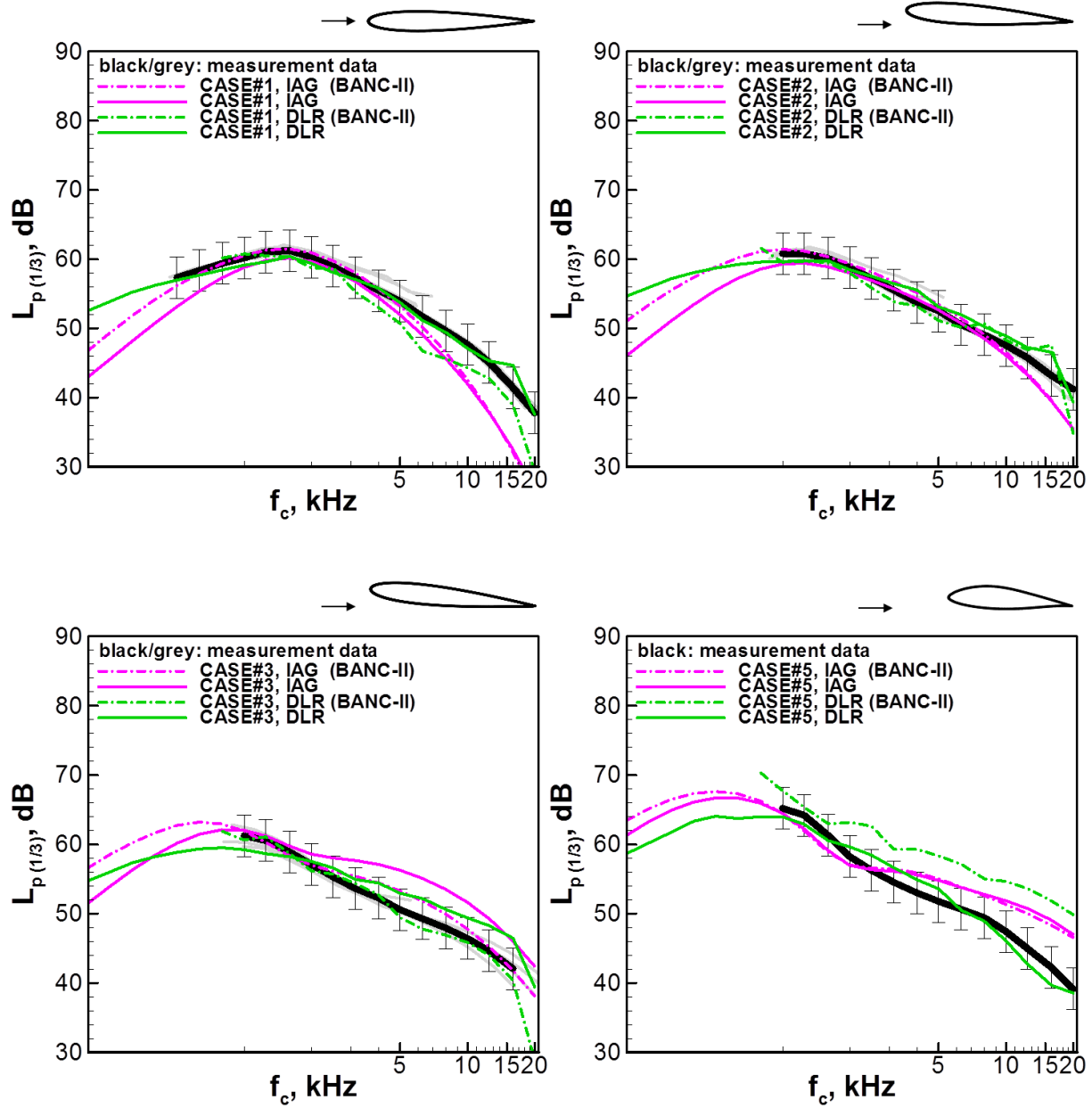
Figure 14. Comparisons of BANC-II-1 and BANC-III-1 farfield TEN results based on the same comparison datasets as in figure 13.

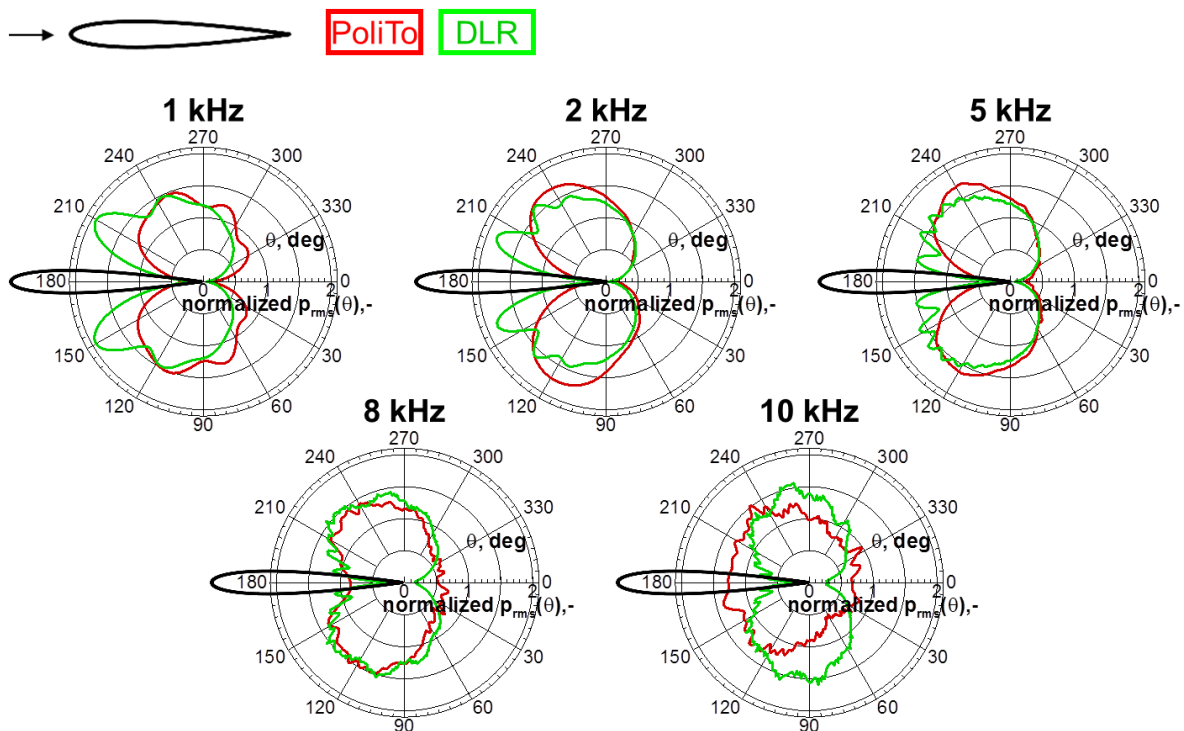American Institute of Aeronautics and Astronautics

Figure 15. 1/3-octave-band representation of predicted normalized farfield noise directivities for case #1 (no experimental validation data available).
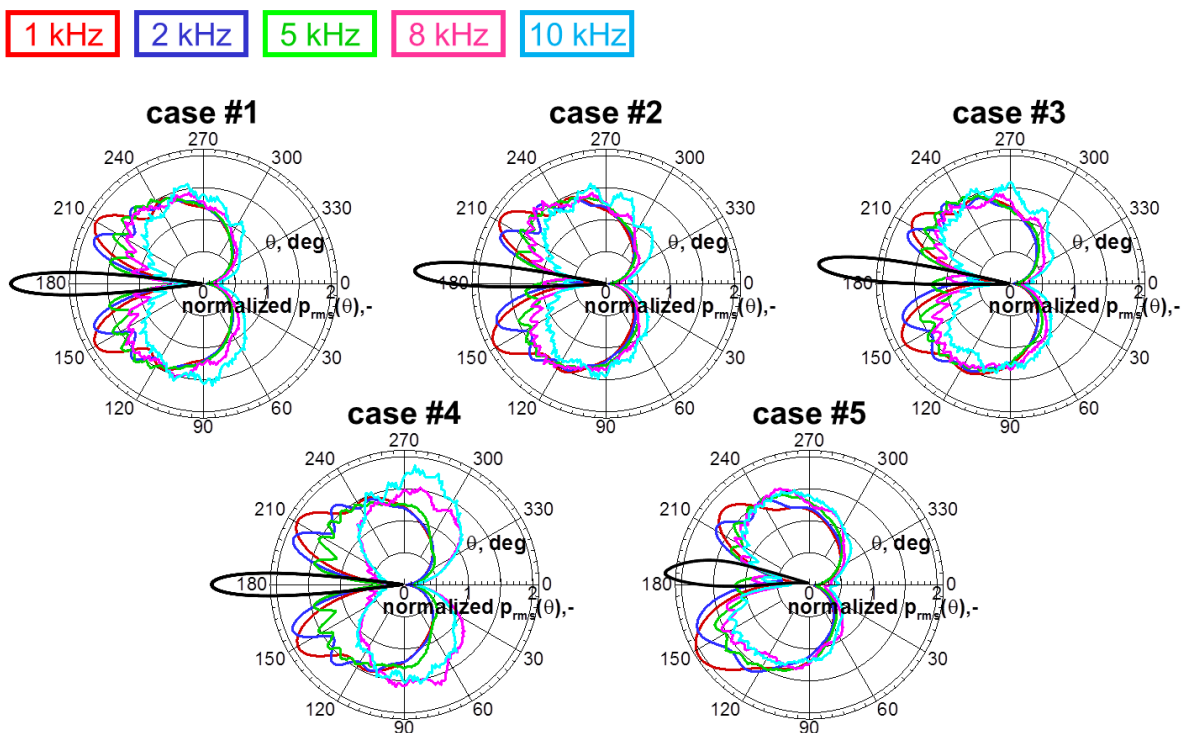

Figure 16. DLR predictions of normalized farfield noise directivities in 1/3-octave-bands for all test cases.

IV.E. Comparison of trend predictions

In the following figures 17 to 21—mainly through reformatting of the already shown datasets— it is surveyed, whether major trends and relative level differences are correctly captured by the predictions.

According to figures 17 and 18, the expected velocity scaling behavior of both farfield TEN and surface pressures is well reproduced by DLR and DTU results. In this comparison DLR predictions perfectly match the measurement data, which is in line with the good prediction quality of k_T for the particular test cases #1 and #4. IAG, however, overpredicts $L_{p(1/3)}(f_c)$ and $G_{pp}(f)$ for case #4; therefore, the trend prediction appears less perfect. Similar observations were already made during BANC-II-1. Particularly, given the very good prediction quality of the near-wake parameters, the reasons for this deviation are currently unclear.

As shown in figure 19, the angle-of-attack behavior of farfield TEN spectra at intermediate- to high frequencies is best predicted by DTU. An overall non-uniform picture of predicted trends in $G_{pp}(f)$ is provided in figure 18; IAG and DTU predict reasonable trends at least for the SS. Finally, figure 21 compares farfield TEN spectra for the NACA0012 and DU96-W-180 airfoils at a given constant α. Here, relative level differences and general trends are best reproduced in the DLR results.
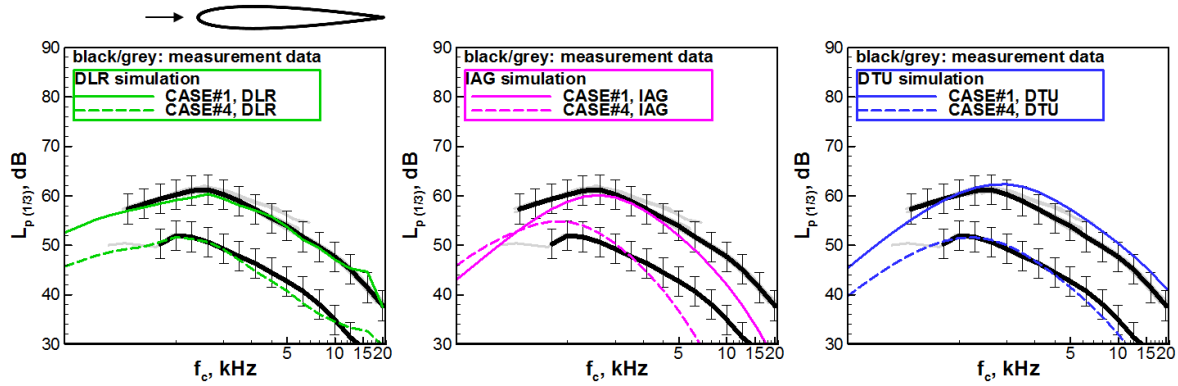

Figure 17. Effect of test velocity on farfield TEN spectra $L_{p(1/3)}(f_c)$ (i. e. cases #1 vs. #4).
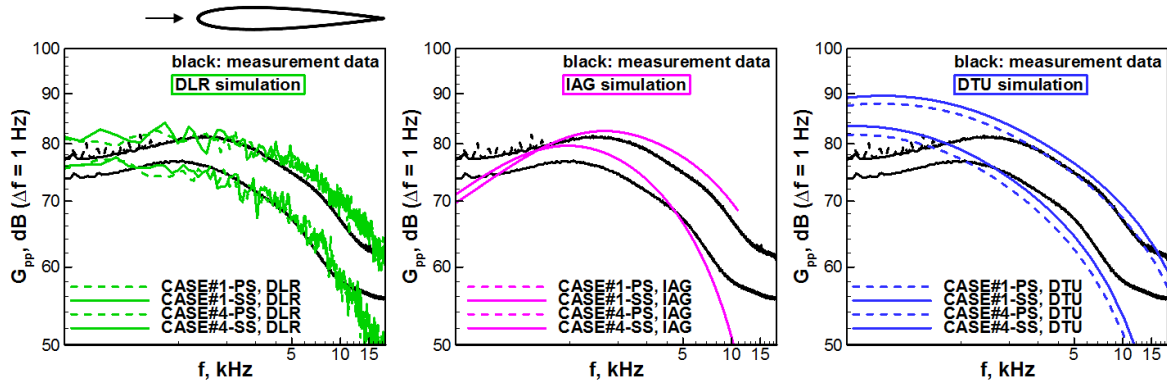

Figure 18. Effect of test velocity on unsteady surface pressure PSDs G_{pp} (i. e. cases #1 vs. #4).
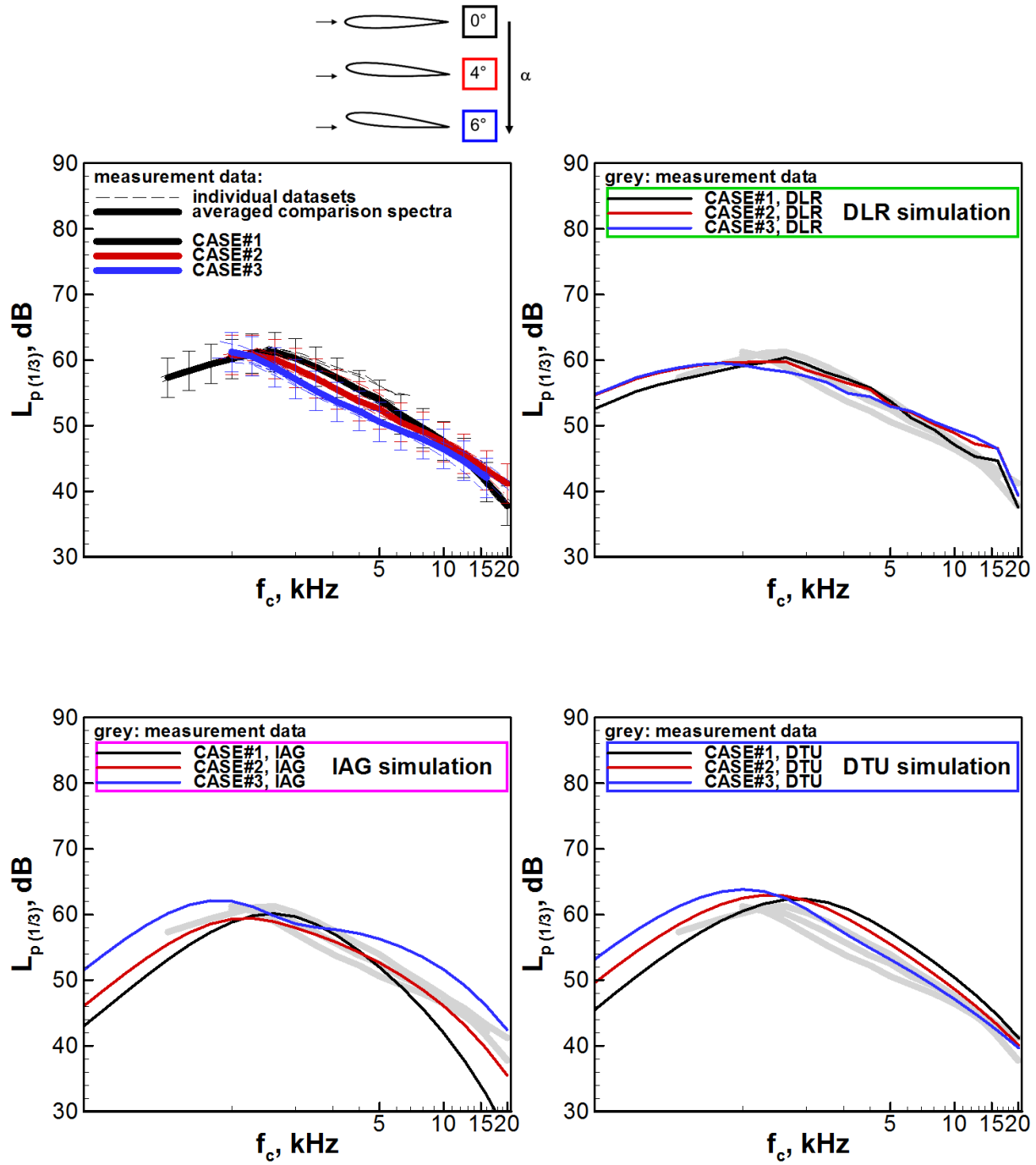
Figure 19. Effect of angle-of-attack on farfield TEN spectra $L_{p(1/3)}(f_c)$ (i. e. cases #1–3).

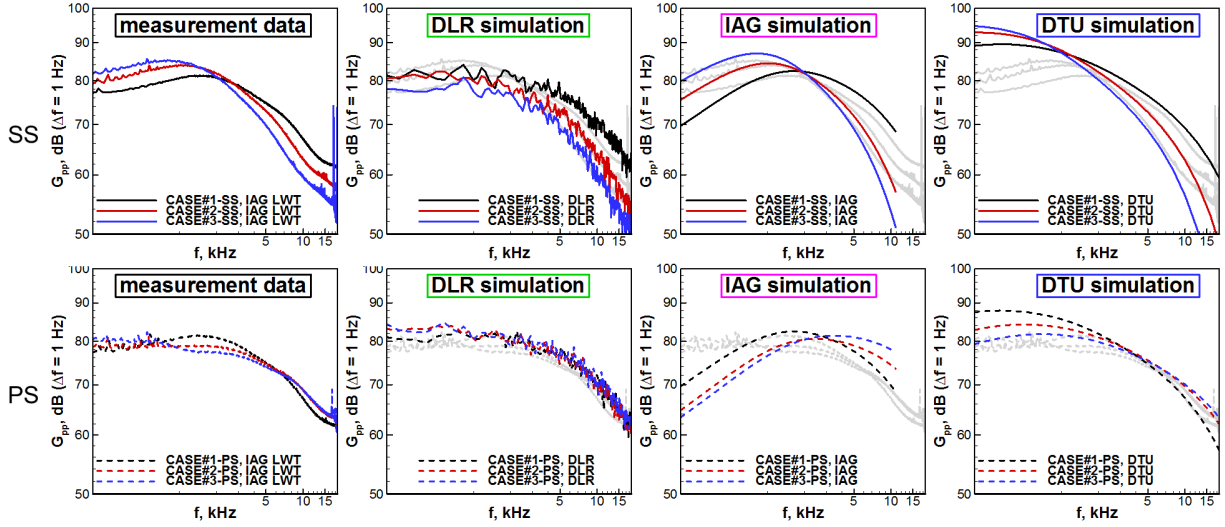American Institute of Aeronautics and Astronautics

Figure 20. Effect of angle-of-attack on unsteady surface pressure PSDs G_{pp} (i.e. cases #1–3).

V. Summary, conclusions and outlook

Computational prediction results for the category 1 BANC-III workshop problem (broadband turbulent boundary-layer trailing-edge noise, TEN) are thoroughly documented herein. Contributions of four scientific groups were submitted, whereof two of them represent new participants with regard to the previous BANC-II workshop in 2012. Still, the number of workshop contributors appears much too low, given the total number of publications on the subject. All presented computational approaches have been developed in an industrial context and provide comparatively low computational expenses. Code-to-code comparisons are shown for the following simulation methods and from the following institutions:

- The University of Stuttgart (IAG, Institute of Aerodynamics & Gas Dynamics) and the Technical University of Denmark (DTU) applied 2D-RANS-based simplified theoretical surface pressure models of the 'Blake-TNO'-type. Here, turbulent boundary-layer quantities are extracted from a CFD/RANS computation and correspondingly predicted surface pressure spectra are fed into a classical (diffraction theory) farfield noise prediction.

- The German Aerospace Center (DLR) contributed results from hybrid RANS-based 2D-CAA simulations, coupled with 3D stochastic source modeling, where fluctuating sources are reconstructed based on the RANS statistics.

- The Politecnico di Torino (PoliTo) in cooperation with wavePRO S.R.L. and Metacomp Technologies, Inc. considered a new strategy, based on a numerical, hybrid RANS/LES (IDDES) of the nearfield noise, coupled with a FWH solution in the farfield. Synthetic turbulence is used to seed resolved-scale turbulence in the boundary layer to provoke the wake unsteadiness which is otherwise not self-initiating for the selected NACA0012 test case. A nominally 3D FWH solver was applied to propagate the noise from a single (effectively 2D-IDDES) slice.

Improvements with regard to BANC-II include the realization of a Liepmann turbulence spectrum in DLR's stochastic source model FRPM, as well as an improved modeling by IAG of the convection velocity and the so-called 'moving axis' spectrum, describing the temporal evolution of vortices within the turbulent boundary-layer.

Overall, the achieved results display a high scientific quality level. In most of the cases farfield TEN predictions are within or very close to the provided data scatter band (reproducing systematic errors between multiple test facilities). TEN maxima are principally well-represented in terms of frequency and level. However, mutual comparisons show individual code-specific advantages and disadvantages, indicating that a methodology which comprehensively predicts all of the requested nearfield and farfield quantities, is not available to date. General trends (like the dependence of farfield noise or surface pressure spectra on angle-of
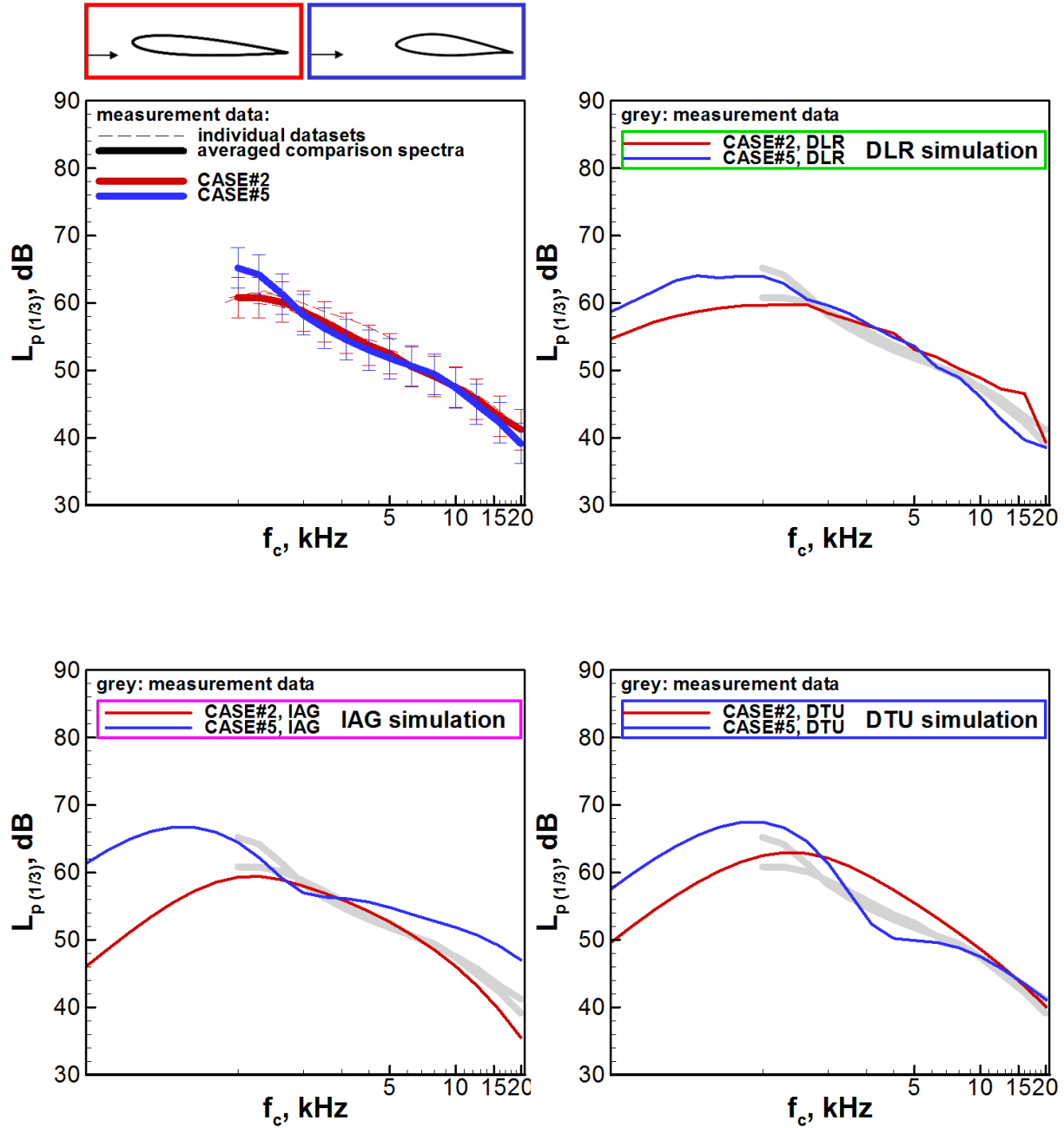
Figure 21. Effect of airfoil geometry on farfield TEN spectra $L_{p(1/3)}(f_c)$ (i.e. cases #2 vs. #5, $\alpha = 4°$).

American Institute of Aeronautics and Astronautics

attack and freestream velocity) are not always correctly represented in the different contributions. Moreover, the very fast farfield noise prediction based on modeled surface pressure spectra is not designed to provide detailed directivity information which was made available only by PoliTo and DLR. To gain a more elaborate overview an increased number of participants from the CAA/LES community is desirable. Note that a weakness in available farfield TEN validation databases consists in lacking experimental information on directivities and for frequencies below ~ 1 kHz. At those frequencies differences in the predicted spectral shapes, particularly the roll-off region below the spectral peaks, will need further clarification. Future experimental work should therefore, consider possibilities to enhance current TEN measurement capabilities.

On the simulation side follow-up activity by PoliTo and DLR will focus on establishing full 3D CAA simulations within acceptable computational costs. With regard to the 'Blake-TNO' approaches a more detailed parameter sensitivity analysis, including dedicated input quantities (like e.g. the normal length scales, normal velocity fluctuations spectra etc.) is recommended. These mutual comparisons should be based on identical RANS solutions to exclude individual dependencies on different CFD results.

The BANC experimental database will be extended by additional test cases and supplementing datasets, provided by DTU Wind Energy and DLR. Specifications will be included in the forthcoming updated version of the problem statement to be issued in preparation of BANC-IV. A mid- to long term perspective for future workshops is seen in the consideration of noise reduction devices as a demanding task for the CAA community. For developers of enhanced 'Blake-TNO' models the treatment of airfoils with moderate flow separation could be another selectable field.

References

[1] BANC collaborative website, URL: https://info.aiaa.org/tac/ASG/FDTC/DG/BECAN_files_/ [cited May 2015].

[2] T. I. Alecu, S. Voloshynovsky, and T. Pun. The Gaussian Transform. EUSIPCO 2005, 13th European Signal Processing Conference, 2005.

[3] P. Batten, U. Goldberg, E. Kang, and S. Chakravarthy. Smart Sub-Grid-Scale Models for LES and Hybrid RANS/LES. AIAA Paper 2011-3472, 2011.

[4] P. Batten, E. Ribaldone, M. Casarella, and S. Chakravarthy. Towards a Generalized Non-Linear Acoustics Solver. AIAA Paper 2004-3001, 2004.

[5] F. Bertagnolio, A. Fischer, and W. J. Zu. Tuning of Turbulent Boundary Layer Anisotropy for Improved Surface Pressure and Trailing-Edge Noise Modeling. *Journal of Sound and Vibration*, 333:991–1010, 2014.

[6] W. K. Blake. Mechanics of Flow-Induced Sound and Vibration, Complex Flow-Structure Interactions. *Applied Mathematics and Mechanics*, 17(II):756–767, Academic Press, Inc., Orlando, FL, 1986.

[7] T. F. Brooks and T. H. Hodgson. Trailing Edge Noise Prediction from Measured Surface Pressures. *Journal of Sound and Vibration*, 78(1):69–117, 1981.

[8] T. F. Brooks, D. S. Pope, and M. A. Marcolini. Airfoil Self-Noise and Prediction. NASA Reference Publication 1218, 1989.

[9] K. L. Chandiramani. Diffraction of Evanescent Waves with Applications to Aerodynamically Scattered Sound and Radiation from Unbaffled Plates. *Journal of the Acoustical Society of America*, 55:19–29, 1974.

[10] D. M. Chase. Modeling the Wavevector-Frequency Spectrum of Turbulent Boundary Layer Wall Pressure. *Journal of Sound and Vibration*, 70(1):29–67, 1980.

[11] M. Choudhari and K. Yamamoto. Integrating CFD, CAA, and Experiments towards Benchmark Datasets for Airframe Noise Problems. 5th Symposium on Integrating CFD and Experiments in Aerodynamics (Integration 2012), JAXA Chofu Aerospace Center, Tokyo, Japan, 3–5 October 2012.

[12] J. W. Delfs, M. Bauer, R. Ewert, H. A. Grogger, M. Lummer, and T. G. W. Lauke. Numerical Simulation of Aerodynamic Noise with DLR's Aeroacoustic Code PIANO, 2008.

[13] M. Dieste and G. Gabard. Random Particle Methods Applied to Broadband Fan Interaction Noise. *J. Comp. Phys.*, 231(24):8133–8151, 2012.

[14] R. Ewert. Acoustic Perturbation Equations Based on Flow Decomposition via Source Filtering. *Journal of Computational Physics*, 188(2):365–398, July 2003.

[15] R. Ewert. RPM—The Fast Random Particle-Mesh Method to Realize Unsteady Turbulent Sound Sources and Velocity Fields for CAA Applications. Technical report, 2007.

[16] R. Ewert. Broadband Slat Noise Prediction Based on CAA and Stochastic Sound Sources from a Fast Random Particle-Mesh (RPM) Method. *Computers & Fluids*, 37:369–387, 2008.

[17] R. Ewert, C. Appel J. Dierke, and M. Herr. RANS/CAA Based Prediction of NACA0012 Broadband Trailing-Edge Noise and Experimental Validation. AIAA Paper 2009-3269, 2009.

[18] R. Ewert, J. Dierke, J. Siebert, A. Neifeld, C. Appel, M. Siefert, and O. Kornow. CAA Broadband Noise Prediction for Aeroacoustic Design. *Journal of Sound and Vibration*, 330(17):4139–4160, August 2011.

[19] R. Ewert and R. Emunds. CAA Slat Noise Studies Applying Stochastic Sound Sources Based on Solenoidal Digital Filters. AIAA Paper 2005-2862, 2005.

[20] R. Ewert, O. Kornow, J.W. Delfs, J. Yin, T. Röber, and M. Rose. A CAA Based Approach to Tone Haystacking. AIAA Paper 2009-3217, 2009.

[21] M. Herr, C. Bahr, and M. Kamruzzaman. Workshop Category 1: Trailing-Edge Noise. Problem Statement for the AIAA/CEAS Second Workshop on Benchmark Problems for Airframe Noise Computations (BANC-II), June 7–8 2012, Colorado Springs, Colorado, USA, URL: https://info.aiaa.org/tac/ASG/FDTC/DG/BECAN_files_/BANCII_category1 [cited May 2015], June 2012.

[22] M. Herr and M. Kamruzzaman. Benchmarking of Trailing-Edge Noise Computations—Outcome of the BANC-II Workshop. AIAA Paper 2013-2123, 2013.

[23] A. Herrig. *Validation and Application of a Hot-Wire based Method for Trailing-Edge Noise Measurements on Airfoils.* Doctoral thesis, Institute of Aerodynamics and Gas Dynamics, Faculty of Aerospace Engineering and Geodesy, University of Stuttgart, Stuttgart, Germany, 2011.

[24] M. S. Howe. A Review of the Theory of Trailing Edge Noise. *Journal of Sound and Vibration*, 61(3):437–465, 1978.

[25] M. S. Howe. *Acoustics of Fluid-Structure Interactions.* Cambridge University Press, 2000.

[26] A. Iob, R. Arina, P. Batten, and S. Chakravarthy. Generating Trailing-Edge Noise Predictions Using Synthetic Turbulence. AIAA Paper 2014-2764, 2014.

[27] M. Kamruzzaman. *Study of Turbulence Anisotropy and its Impact on Flow Induced Noise Emission.* Doctoral thesis, Institute of Aerodynamics and Gas Dynamics, Faculty of Aerospace Engineering and Geodesy, University of Stuttgart, Stuttgart, Germany, 2011.

[28] M. Kamruzzaman, D. Bekiropoulos, A. Wolf, T. Lutz, and E. Krämer. Rnoise: A RANS Based Airfoil Trailing-Edge Noise Prediction Model. AIAA Paper 2014-3305, 2014.

[29] M. Kamruzzaman, T. Lutz, A. Herrig, and E. Kraemer. Semi-Empirical Modeling of Turbulent Anisotropy for Airfoil Self Noise Prediction. *AIAA Journal*, 50(1):46–60, 2012.

[30] M. Kamruzzaman, T. Lutz, W. Würz, and E. Kraemer. On the Length Scales of Turbulence for Aeroacoustic Applications. AIAA Paper 2011-2734, 2011.

[31] D. A. Lynch, W. K. Blake, and T. J. Mueller. Turbulence Correlation Length-Scale Relationships for the Prediction of Aeroacoustics Response. *AIAA J.*, 43(6):1187–1197, 2005.

[32] F. R. Menter. Two-Equation Eddy-Viscosity Turbulence Models for Engineering Applications. *AIAA Journal*, 32(8):1598–1605, 1994.

[33] J. A. Michelsen. Basis3D - A Platform for Development of Multiblock PDE Solvers. Technical Report AFM 92-05, Technical University of Denmark, Lyngby, Denmark, 1992.

[34] J. A. Michelsen. Block Structured Multigrid Solution of 2D and 3D Elliptic PDE's. Technical Report AFM 94-06, Technical University of Denmark, Lyngby, Denmark, 1994.

[35] R. Parchen. Progress Report DRAW: A Prediction Scheme for Trailing Edge Noise Based on Detailed Boundary-Layer Characteristics. Report of the TNO (The Netherlands Organization) Institute of Applied Physics HAG-RPT-980023, Feb. 1998.

[36] R .J. Purser, W.-S. Wu, D. F. Parrish, and N. M. Roberts. Numerical Aspects of the Application of Recursive Filters to Variational Statistical Analysis. Part I: Spatially Homogeneous and Isotropic Gaussian Covariances. *Monthly Weather Review*, 131:15241535, 2003.

[37] R. J. Purser, W.-S. Wu, D. F. Parrish, and N. M. Roberts. Numerical Aspects of the Application of Recursive Filters to Variational Statistical Analysis. Part II: Spatially Inhomogeneous and Ansiotropic General Covariances. *Monthly Weather Review*, 131:15361548, 2003.

[38] C. Rautmann, J. Dierke, R. Ewert, N. Hu, and J. Delfs. Generic Airfoil Trailing-Edge Noise Prediction using Stochastic Sources from Synthetic Turbulence. AIAA Paper 2014-3298, 2014.

[39] N. Reiche, M. Lummer, and R. Ewert. Towards High-Lift Noise from Fast Multipole BEM with Anisotropic Synthetic Turbulence Sources. AIAA Paper 2014-tbd, 2015.

[40] K. S. Rossignol and M. Herr. Previously unpublished data acquired by DLR Braunschweig (GE proprietary, released for BANC-II and follow-on workshops by courtesy of GE Wind Energy), 2011.

[41] M. L. Shur, P. R. Spalart, M. K. Strelets, and A. K. Travin. A Hybrid RANS-LES Approach with Delayed-DES and Wall-Modelled LES Capabilities. *International Journal of Heat and Fluid Flow*, 29:1638–1649, 2008.

[42] M. Siefert and R. Ewert. Sweeping Sound Generation in Jets Realized with a Random Particle-Mesh Method. AIAA Paper 2009-3369, 2009.

[43] N. N. Sørensen. General Purpose Flow Solver Applied to Flow over Hills. PhD Thesis, Tech. Rep. Risø-R-827(EN), Risø National Laboratory, Roskilde, Denmark, June 1995.

[44] C. Tam and J. Webb. Dispersion-Relation-Preserving Finite Difference Schemes for Computational Acoustics. *J. Comp. Phys.*, 107:262–281, 1993.

[45] A. Wohlbrandt, N. Hu, S. Guerin, and R. Ewert. Generalised Turbulence Spectra for Broadband Noise Predictions with the Random Particle Mesh Method. *submitted to Journal of Sound and Vibration*, 2015.

[46] I. T. Young and L. J. van Vliet. Recursive Implementation of the Gaussian Filter. *Signal Processing*, 44:139–151, 1995.